International Journal of Heat and Fluid Flow 118 (2026) 110227

Contents lists available at ScienceDirect

International Journal of Heat and Fluid Flow

journal homepage: www.elsevier.com/locate/ijhff

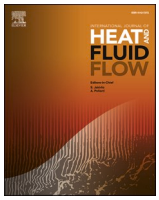

Mathematical regulation of Gyroid-type TPMS structures for enhanced convective heat transfer

Kaiwen Qin [a,b], Si Yang [a,b], Tingxiang Lv [a,b], Xijun Zhao [a,b], Xiaobin Tang [a,b,*]

[a] Department of Nuclear Science and Technology, Nanjing University of Aeronautics and Astronautics, Nanjing 211106, China
[b] Key Laboratory of Advanced Nuclear Technology and Radiation Protection, Ministry of Industry and Information Technology, Nanjing 211106, China

ARTICLE INFO

Keywords:
Gyroid structure
Amplitude control
Periodicity control
Phase control
Enhanced heat transfer

ABSTRACT

Triply periodic minimal surface (TPMS) structures have demonstrated significant potential for enhanced heat transfer owing to their compact structural design and excellent effective thermophysical properties. To further improve their convective heat transfer performance, precise control over their morphology has become a focus in current studies. In this study, a Gyroid-type TPMS structure was selected as the research subject, and three functional improvement methods—amplitude control, periodicity control, and phase control—were proposed. The effects of different control strategies on the morphological characteristics of the Gyroid structure were analyzed, and the flow and heat transfer characteristics of the improved Gyroid structure were calculated by numerical simulation and experimental measurement. The results show that with increasing values of the through-hole control factor (α), the peak temperature (T_{max}) of the Gyroid structure decreases by 19.0–33.6 K, while the convective heat transfer coefficient (h) increases by 29.4–33.7 %. Similarly, with increasing values of the wrinkle control factor (β), T_{max} decreases by 7.3–8.8 K, h increases by 5.4–7.9 %. The proposed methods not only provide a novel idea for further enhancing the heat transfer performance of Gyroid structures, but also offer valuable reference and theoretical support for the optimal design of other TPMS structures.

1. Introduction

In recent years, architected porous materials have attracted growing attention across thermal and energy-related applications, including flow and heat-transfer regulation in lattice structures (Sun et al., 2025), structural optimization of compact heat exchangers (Wang et al., 2023), and porous media used in combustion, phase-change thermal storage, and packed-bed systems (Dong et al., 2025; Lv et al., 2024; Wang et al., 2025). These studies collectively highlight the broad relevance and engineering importance of porous structures in thermal management. Among various architected porous structures, triply periodic minimal surface (TPMS) structures based on mathematical topology optimization theory have been extensively investigated owing to their unique geometric characteristics and excellent effective thermodynamic properties (Gado et al., 2024; Cheng et al., 2021; Barakat and Sun, 2024; Wang et al., 2023; Qiu et al., 2024). Compared with conventional truss or honeycomb structures, TPMS structures generate continuous, smooth, and infinitely extendable periodic surfaces via differential geometry algorithms. Their zero mean curvature and continuously connected topology in three-dimensional (3D) space not only ensure high interconnectivity for their pore structure but also offer ultrahigh specific surface areas and low-curvature flow channels (Feng et al., 2022; Fisher et al., 2022; Yoo, 2014; Yeranee and Rao, 2022). This porous system, which combines a mathematical topology with biomimetic advantages, demonstrates wide application potential in fields such as aerospace, engineering mechanics, biomedicine, and enhanced heat transfer (Zhang et al., 2025; Feng et al., 2023; Dong and Zhao, 2021; Kaur and Singh, 2021; Yang et al., 2024). In the field of enhanced heat transfer, TPMS structures, which have tunable topological properties, can not only optimize heat flow distribution and reduce thermal resistance but also enhance the turbulence effect in convective heat transfer (Piedra et al., 2023; Yeranee et al., 2024), thereby providing revolutionary technical solutions for the design of next-generation high-efficiency heat exchangers, electronic-device cooling technologies, and high-power heat sinks.

At present, numerous scholars have conducted studies on the flow and heat transfer performance of TPMS structures. Wang et al. (2023) numerically evaluated helium flow and heat transfer in several TPMS channel structures and showed that TPMS geometries provide significantly higher heat-transfer performance than conventional straight

* Corresponding author at: Department of Nuclear Science and Technology, Nanjing University of Aeronautics and Astronautics, Nanjing 211106, China.
E-mail address: tangxiaobin@nuaa.edu.cn (X. Tang).

https://doi.org/10.1016/j.ijheatfluidflow.2025.110227
Received 20 August 2025; Received in revised form 3 December 2025; Accepted 22 December 2025
Available online 27 December 2025

channels, with F-KS offering the best overall thermal–hydraulic performance among the tested structures. Li et al. (2020) designed Gyroid- and Schwarz-D-type TPMS heat exchangers for supercritical CO_2 Brayton cycles and, compared with a conventional zigzag PCHE, showed 30–80 % higher heat-transfer coefficients and 15–100 % better overall thermal performance at the expense of 50–100 % higher pressure drop. Iyer et al. (2022) numerically compared seven TPMS heat-exchanger structures and found that all provide higher heat-transfer coefficients than a traditional tubular channel, with the Schwarz-D structure exhibiting the best overall thermal–hydraulic performance. Ma et al. (2025) proposed a double-wall cooling design based on Primitive-type TPMS structures, which compared with the traditional pin–fin configuration—enhances the internal convective heat transfer of the double-wall channel by up to 57.9 % and improves the overall cooling effectiveness by more than 10 %. Zuo et al. (2025) applied Gyroid-type TPMS structures as effusion holes at the leading edge of a gas turbine blade, yielding a 2.1 %–9.3 % increase in cooling effectiveness and a more uniform surface temperature distribution at high blowing ratios. Yeranee et al. (2024) used topology optimization to design Diamond-type TPMS structures for gas-turbine blade trailing-edge channels, achieving a 139.7 %–150.2 % improvement in thermal performance over pin-fins.

Numerous studies have demonstrated the significant advantages of TPMS structures for enhancing heat transfer (Wang et al., 2023; Li et al., 2020; Iyer et al., 2022; Ma et al., 2025; Zuo et al., 2025; Yeranee et al., 2024). However, the heat transfer performance of standard TPMS structures remains limited, and many studies have focused on improving it through morphological control. Tang et al. (2023) investigated convective heat transfer using a combination of numerical simulations and experiments, with emphasis on three types of TPMS structures: Gyroid, Diamond, and IWP. Their results showed that the Gyroid and IWP structures exhibited “through-hole” features in the planar view (as shown in Fig. 1(a)). The presence of “through-holes” causes the fluid to preferentially flow through low-resistance regions, thus reducing the heat transfer between the solid surface and fluid, which is disadvantageous for convective heat transfer. Si et al. (2025) proposed a lattice-scale topology optimization method for TPMS heat sinks, reconstructing the originally uniform periodic TPMS structure into a three-dimensional non-uniform porous lattice. By adjusting a finite set of geometric parameters in the TPMS equation, the method increases the solid fraction and thickens the lattice near the heating region to enhance heat conduction, while creating larger pores in regions away from the heat source to reduce flow resistance, thereby achieving coordinated thermal–fluid performance optimization without compromising structural connectivity or manufacturability. Xiao et al. (2025) proposed a method that modifies the implicit equation of the Gyroid to regulate its local curvature and amplitude, thereby constructing structures with convex features and concave–convex composite features on the basis of the original Gyroid geometry. Numerical results show that these convex and concave–convex structures can significantly alter flow separation and enhance secondary flow intensity, strengthening fluid impingement and attachment on the walls. Under typical operating conditions, compared with the standard Gyroid, their heat transfer capabilities are enhanced by approximately 9 %–16 % and 17 %–29 %, respectively. Tang et al. (2024) proposed a configuration method that incorporates adjustable fins into Gyroid-type TPMS, thereby forming finned geometries within the internal flow channels of the Gyroid structure. Numerical results indicate that increasing the fin height enhances flow disturbance and enlarges the heat-transfer area, leading to a 27.4 %–34.6 % improvement in heat-transfer performance and a reduction in temperature rise by approximately 9.8–9.9 °C. However, the pressure drop increases significantly at the same time, with an increment of 14.7 %–108.4 %. Furthermore, Qin et al. (2025) previously proposed two types of TPMS structures for heat exchangers: Gyroid and Diamond structures. Using oxygen-free pure copper powder, they fabricated these complex structures on a 3D printer via selective laser melting (SLM) technology. The surface of the 3D-printed Gyroid structure was not mirror-smooth but exhibited a certain degree of roughness (as shown in Fig. 1(b)). This microscopic surface roughness promotes fluid mixing and was found to enhance the heat transfer efficiency. These studies show that precise morphological control of TPMS structures provides an effective approach to enhancing convective heat transfer.

As known from the aforementioned research, reducing the “through-holes” in TPMS structures and increasing their surface roughness can enhance fluid mixing and improve convective heat transfer. Therefore, it is envisioned in this study that if the TPMS function equation can be precisely controlled, allowing the “through-holes” in the TPMS structure to close and the TPMS structure surface to no longer be smooth, then theoretically, it would be possible to further enhance fluid mixing and improve convective heat transfer based on the standard TPMS structure. Based on this idea, three functional improvement methods—amplitude control, periodicity control, and phase control—were proposed in this study to precisely control the closure of “through-holes” and the formation of “wrinkle-like” geometric features in the Gyroid structure. The effects of different control strategies on the morphological characteristics of the Gyroid structure were analyzed, and the flow and heat transfer characteristics of the improved Gyroid structure were numerically calculated. Furthermore, an experimental setup was designed to validate the accuracy of the numerical simulation method. These methods not only provide effective approaches for improving the Gyroid structure but also offer important references and theoretical support for the optimal design of other TPMS structures.

2. TPMS function control method

TPMS can be mathematically represented using trigonometric functions, and the trigonometric function for TPMS is expressed as follows (Gandy et al., 2001):

$$F(r) = \sum_{k=1}^{K} A_k \cos\left[\frac{2\pi r}{L_k} + \varphi_k\right] = C \tag{1}$$

where A_k, L_k, φ_k denote the amplitude, period, and phase parameters,

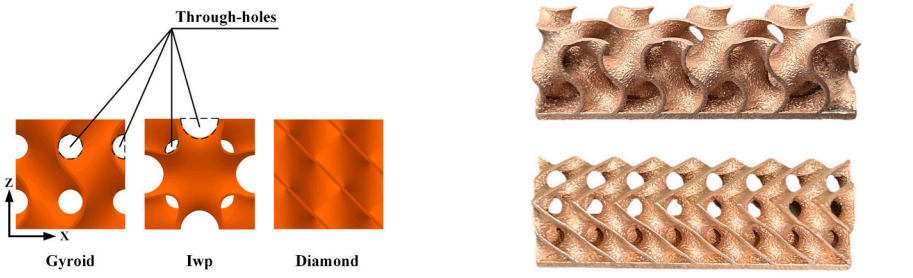

(a) through-holes structure[23]

(b) 3D-printed Gyroid and Diamond structure[29]

Fig. 1. TPMS “through-hole” structure and 3D printed physical diagram.

respectively, C is the offset of the unit surface, K is the number of trigonometric functions, and r is the linear combination of the three-dimensional spatial coordinates (x,y,z).

These parameters (amplitude, period, and phase) collectively determine the pore-unit shape, pore size, porosity, and topological characteristics of TPMS structures (Liu et al., 2024). To achieve localized geometric regulation and spatial topological variation within a TPMS framework, these parameters must be appropriately adjusted within the implicit function so that different regions of the structure exhibit distinct morphological features while the overall functional form remains unchanged.

Based on this concept, this study adopts three function-control strategies—amplitude control, periodicity control, and phase control—to locally regulate the morphology of the Gyroid structure by adjusting the amplitude, period, and phase parameters, respectively. More detailed mathematical formulations and the corresponding morphological variations of these control methods are presented in the following sections.

3. Effects of different control methods on Gyroid structure

3.1. Amplitude control

The Gyroid-type TPMS structure was selected as the research subject for this study. It is mathematically expressed by the following trigonometric function (Qin et al., 2025):

$$F(r) = \cos(\frac{2\pi}{L}x)\sin(\frac{2\pi}{L}y) + \cos(\frac{2\pi}{L}y)\sin(\frac{2\pi}{L}z) + \cos(\frac{2\pi}{L}z)\sin(\frac{2\pi}{L}x) \quad (2)$$

An improved mathematical expression for the Gyroid function is proposed to achieve precise control over the morphology of the Gyroid structure, as follows:

$$F(r) = A(r)\cos(\frac{2\pi}{L}x)\sin(\frac{2\pi}{L}y) + B(r)\cos(\frac{2\pi}{L}y)\sin(\frac{2\pi}{L}z) + C(r)\cos(\frac{2\pi}{L}z)\sin(\frac{2\pi}{L}x) \quad (3)$$

In the study of functions composed of the products of trigonometric functions, considering that $\cos(x)\sin(y)$, $\cos(y)\sin(z)$, and $\cos(z)\sin(x)$ exhibit similar mathematical structures, i.e., each being a product of cosine and sine functions with cyclic symmetry in the variables, we selected $\cos(x)\sin(y)$ as a representative term for analysis. Specifically, the coefficients $B(r)$ and $C(r)$ were set to a constant value of 1, and the unit length L was set to 10 mm, whereas only $A(r)$ was varied to analyze its effect on the morphology of the Gyroid structure.

When the value of $A(r)$ is a constant A, to preserve the characteristic features of the standard Gyroid function, A is constrained within the range $0.25 \leq |A| \leq 2.00$ (note that this range serves as an approximate reference instead of a strict limitation). Variations in the Gyroid structure for different values of A are shown in Fig. 2 (The TPMS structures were generated using Python by parsing the implicit TPMS function to obtain the initial surface, offsetting this surface along the normal direction to construct the inner and outer TPMS layers, and then

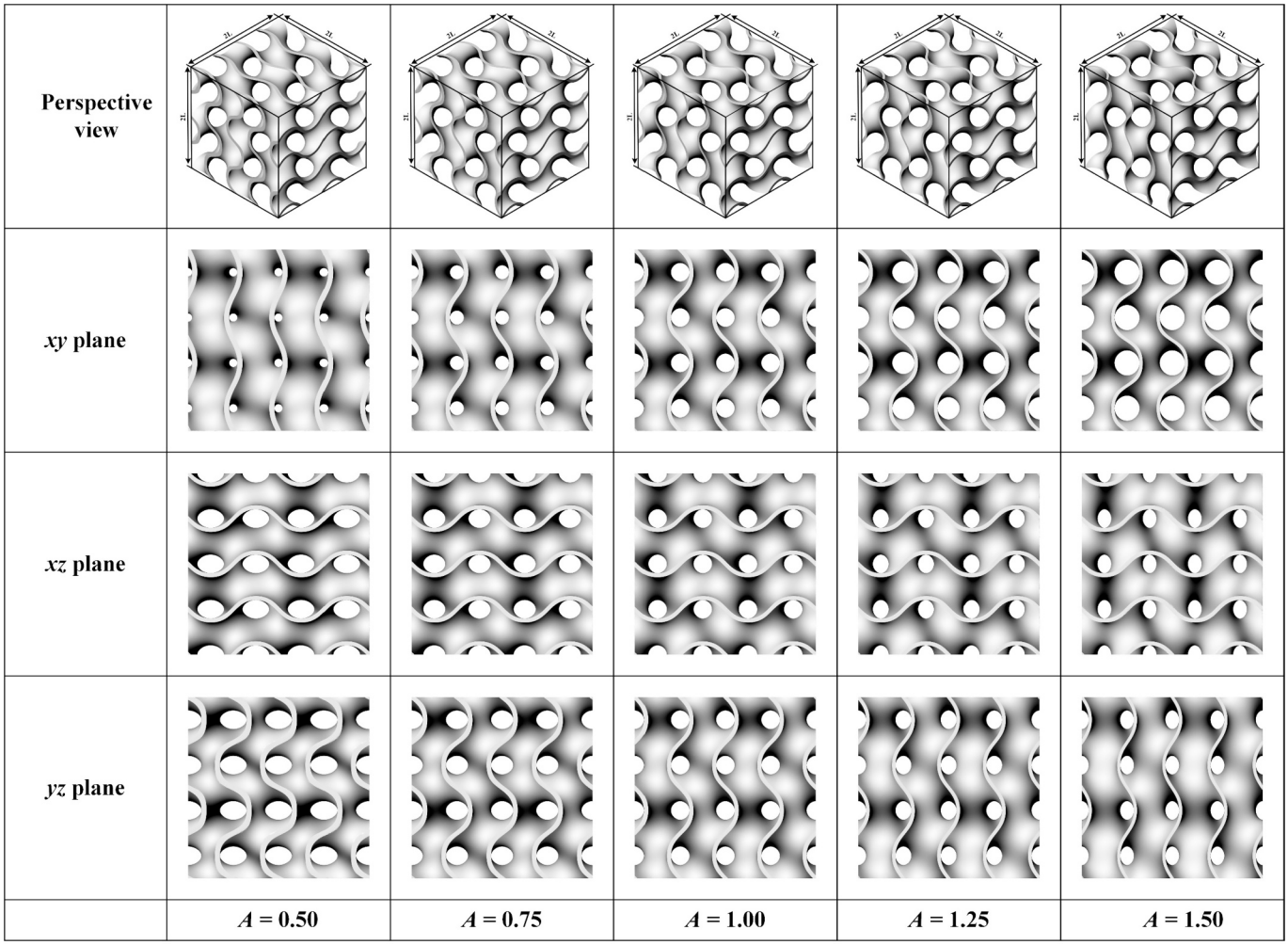

Fig. 2. Variations in the Gyroid structure for different values of A.

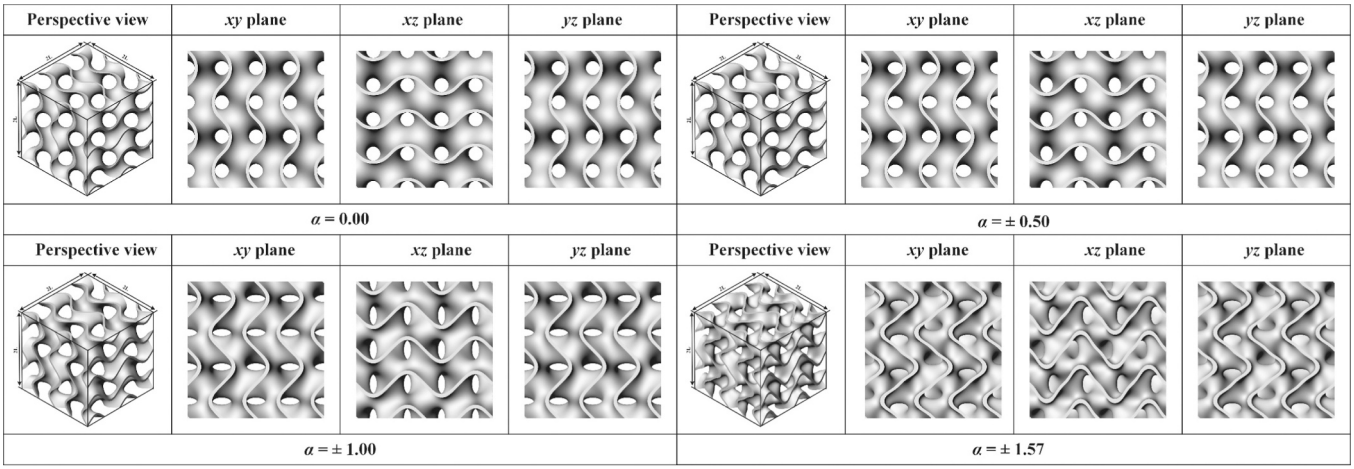

Fig. 3. Effects of different values of α on the Gyroid structure ($A(r) = \cos(\alpha \cdot \sin(z))$).

connecting the corresponding vertices of the two layers to form a closed TPMS structure. In this process, the offset parameter C in Eq. (1) was set to $\pm$ 0.25 to generate the inner and outer TPMS surfaces, corresponding to a wall thickness of 0.5 mm). When $|A| = 1.00$, the pores of the Gyroid structure appeared circular in the *xy*, *xz*, and *yz* plane views, thus indicating isotropy in all directions. For $0.25 \leq |A| < 1.00$, the pores in the *xy* plane decreased gradually in size while retaining a circular shape. Owing to this contraction in the *xy* plane, the pores in the *xz* and *yz* planes were slightly enlarged and transitioned from circular to elliptical shapes, with the long axis along the *z*-direction. When $1.00 < |A| \leq 2.00$, the pores in the *xy* plane increased gradually but maintained their circular form. Owing to this expansion in the *xy* plane, the pores in the *xz* and *yz* planes contracted slightly and shifted from being circular to elliptical, with the short axis along the *z*-direction.

These results indicate that *A* primary affects the size of pores in the *xy* plane, whereas changes in the morphology of the pores in the *xz* and *yz* planes occur indirectly. This phenomenon can be attributed to the fact that $A(r)$ acts only on the $\cos(x)\sin(y)$ term, thereby directly affecting the structural characteristics of the *xy* plane. Similarly, $B(r)$ primarily affects the pore size in the *yz* plane, whereas $C(r)$ affects that in the *xz* plane. When these two parameters are changed simultaneously, such as setting $A(r)$ and $B(r)$ to 2.00, the resulting effect is equivalent to setting $C(r)$ to 0.50. Furthermore, when $A(r)$, $B(r)$, and $C(r)$ are all set to 2.00, the effect is equivalent to the standard Gyroid ($A(r)$, $B(r)$, and $C(r)$ being equal to 1.00). Therefore, when $A(r)$, $B(r)$, and $C(r)$ are constant, only the size of the pores in the corresponding directions is controlled.

When $A(r)$ is non-constant, it should be composed of trigonometric functions to ensure the continuity and smoothness of the Gyroid surface. Additionally, to effectively reduce the internal pore size of the Gyroid structure and thereby enhance heat transfer performance, the range of $A(r)$ should be constrained within $0.00 < A(r) \leq 1.00$. To precisely control the morphological characteristics of the Gyroid structure, a control factor α is introduced, which forms control terms such as $\cos(\alpha \cdot f(r))$ or $\sin(\alpha \cdot f(r))$. The range of α varies depending on the form of $f(r)$.

If $A(r)$ is of the form $\cos(\alpha \cdot f(r))$, then the function $f(r)$ may be set as any trigonometric function or a higher-order nested trigonometric function, including $\sin(z)$, $\sin(z)\cos(z)$, $\sin(\cos(z))$, and $\sin(\cos(\sin(z)))$, among others.

(a) When $f(r) = \sin(z)$, the range of α is constrained to $-1.57 < \alpha < 1.57$, and the effects of α on the Gyroid structure are shown in Fig. 3. The improved Gyroid function is expressed mathematically as follows:

$$\begin{aligned} F(r) = {} & \cos(\frac{2\pi}{L}x)\sin(\frac{2\pi}{L}y)\cos(\alpha \cdot \sin(\frac{2\pi}{L}z)) + \\ & \cos(\frac{2\pi}{L}y)\sin(\frac{2\pi}{L}z)\cos(\alpha \cdot \sin(\frac{2\pi}{L}x)) + \\ & \cos(\frac{2\pi}{L}z)\sin(\frac{2\pi}{L}x)\cos(\alpha \cdot \sin(\frac{2\pi}{L}y)) \end{aligned} \tag{4}$$

(b) When $f(r) = \sin(\cos(z))$, the range of α is constrained to $-1.867 < \alpha < 1.867$, and the effects of α on the Gyroid structure are shown in Fig. 4.

If $A(r)$ is of the form $\sin(\alpha \cdot f(r))$, then the function $f(r)$ should be at least a second-order nested cosine function, such as $\cos(\sin(z))$, $\cos(\cos(z))$, and $\cos(\sin(\cos(z)))$.

(c) When $f(r) = \cos(\sin(z))$, the range of α is constrained to $0.00 < \alpha < 3.14$, and the effects of α on the Gyroid structure are shown in Fig. 5.

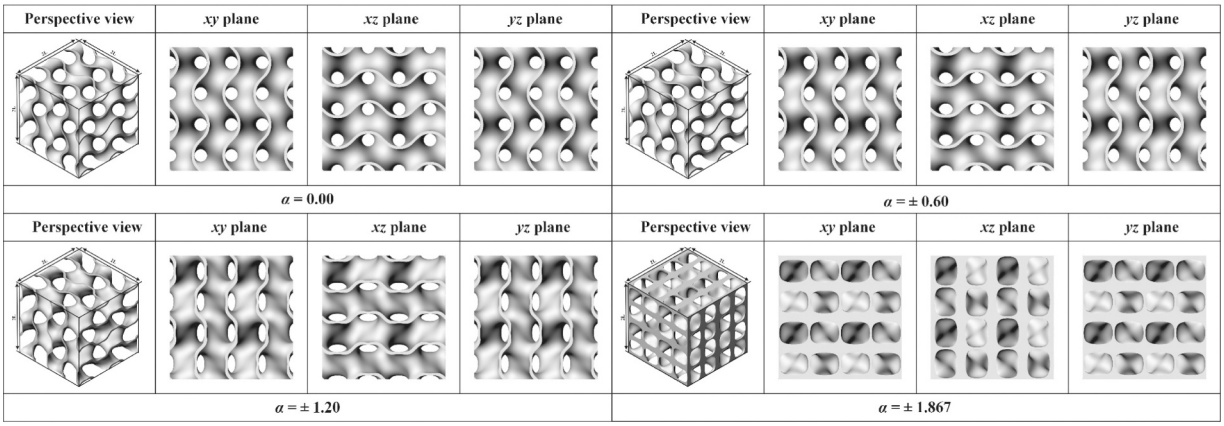

Fig. 4. Effects of different α values on the Gyroid structure ($A(r) = \cos(\alpha \cdot \sin(\cos(z)))$).

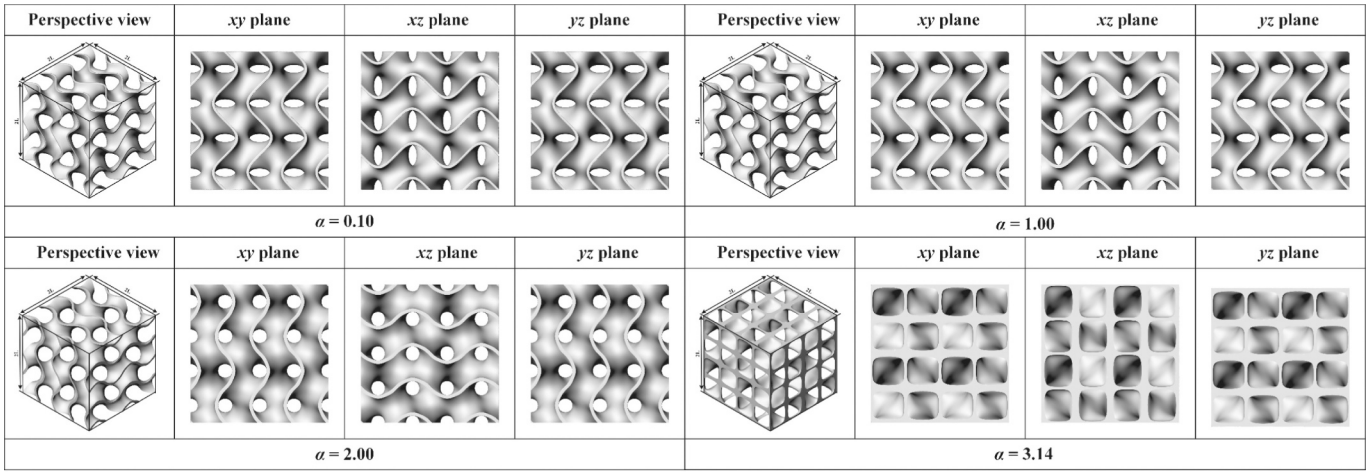

Fig. 5. Effects of different α values on the Gyroid structure ($A(r) = \sin(\alpha \cdot \cos(\sin(z)))$).

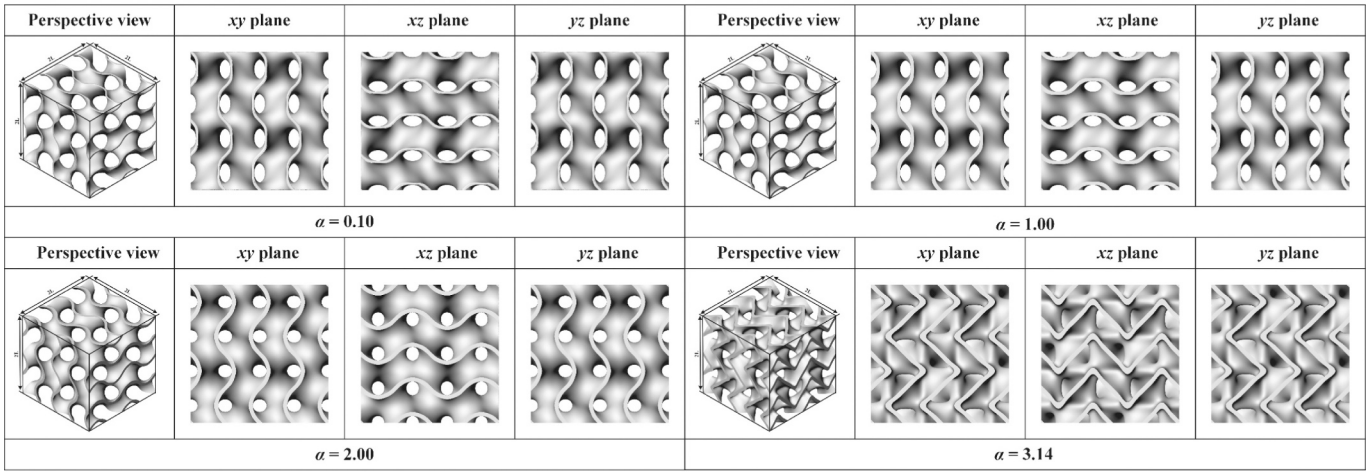

Fig. 6. Effects of different α values on the Gyroid structure ($A(r) = \sin(\alpha \cdot \cos(\sin(\cos(z))))$).

The improved Gyroid function is expressed as follows:

$$\begin{aligned} F(r) = &\cos(\frac{2\pi}{L}x)\sin(\frac{2\pi}{L}y)\sin(\alpha\cdot\cos(\sin(\frac{2\pi}{L}z)))+ \\ &\cos(\frac{2\pi}{L}y)\sin(\frac{2\pi}{L}z)\sin(\alpha\cdot\cos(\sin(\frac{2\pi}{L}x)))+ \\ &\cos(\frac{2\pi}{L}z)\sin(\frac{2\pi}{L}x)\sin(\alpha\cdot\cos(\sin(\frac{2\pi}{L}y))) \end{aligned} \tag{5}$$

(d) When $f(r) = \cos(\sin(\cos(z)))$, the range of α is constrained to $0.00 < \alpha < 3.14$, and the effects of α on the Gyroid structure are shown in Fig. 6.

As shown, whether $A(r)$ is of the form $\cos(\alpha \cdot f(r))$ or $\sin(\alpha \cdot f(r))$, by adjusting the value of α, the pores of the Gyroid structure in the xy, xz, and yz planes can be gradually reduced in size. Simultaneously, the pore shape evolved from elliptical to circular and subsequently reverted to elliptical. Notably, when $A(r)$ is defined as $\cos(\alpha \cdot \sin(z))$, the structural characteristics of the Gyroid function are better preserved, and the adjustment of these features is more convenient.

The analysis above primarily focuses on the case in which $A(r)$ is a linear trigonometric function, which aim to precisely regulate the pore size and shape of the Gyroid structure. To further precisely control the structural morphology of the Gyroid function, subsequent research will explore $A(r)$ in the form of higher-power trigonometric functions ($\cos(\beta \cdot \sin(z^n))$ as an example), such as $\cos(\beta \cdot \sin(z^2))$, $\cos(\beta \cdot \sin(z^3))$, and $\cos(\beta \cdot \sin(z^4))$, among others.

(e) When $A(r) = \cos(\beta \cdot \sin(z^2))$, the improved Gyroid function is expressed mathematically as follows:

$$\begin{aligned} F(r) = &\cos(\frac{2\pi}{L}x)\sin(\frac{2\pi}{L}y)\cos(\beta\cdot\sin(\frac{2\pi}{L}z^2))+ \\ &\cos(\frac{2\pi}{L}y)\sin(\frac{2\pi}{L}z)\cos(\beta\cdot\sin(\frac{2\pi}{L}x^2))+ \\ &\cos(\frac{2\pi}{L}z)\sin(\frac{2\pi}{L}x)\cos(\beta\cdot\sin(\frac{2\pi}{L}y^2)) \end{aligned} \tag{6}$$

To maintain the structural characteristics of Gyroid function, the range of β was set to $-0.628 \le \beta \le 0.628$, and the effects of β on the Gyroid structure are shown in Fig. 7.

(f) When $A(r) = \cos(\beta \cdot \sin(z^3))$, the range of β is set to $-0.628 \le \beta \le 0.628$, and the effects of β on the Gyroid structure are shown in Fig. 8.

As shown in Figs. 7 and 8, in contrast to linear trigonometric functions, which reduce the size of pores in the Gyroid structure, higher-power trigonometric functions can induce the formation of distinct stripe-shaped "wrinkles" on the surface of the Gyroid structure. This "wrinkled" morphology significantly enhances the surface area available for heat transfer, thereby increasing the contact area between the fluid and solid surface. Moreover, this structure disrupts the stability of the fluid boundary layer, which facilitates enhanced fluid mixing and thus increases the overall heat exchange efficiency. As the exponent n increases, the effect of the parameter β on the Gyroid structure reflects a pattern similar to that of a quadratic trigonometric function, without exhibiting a significant variation trend. Notably, this study primarily analyzes the function form $A(r) = \cos(\beta \cdot \sin(z^n))$ as an example. In fact,

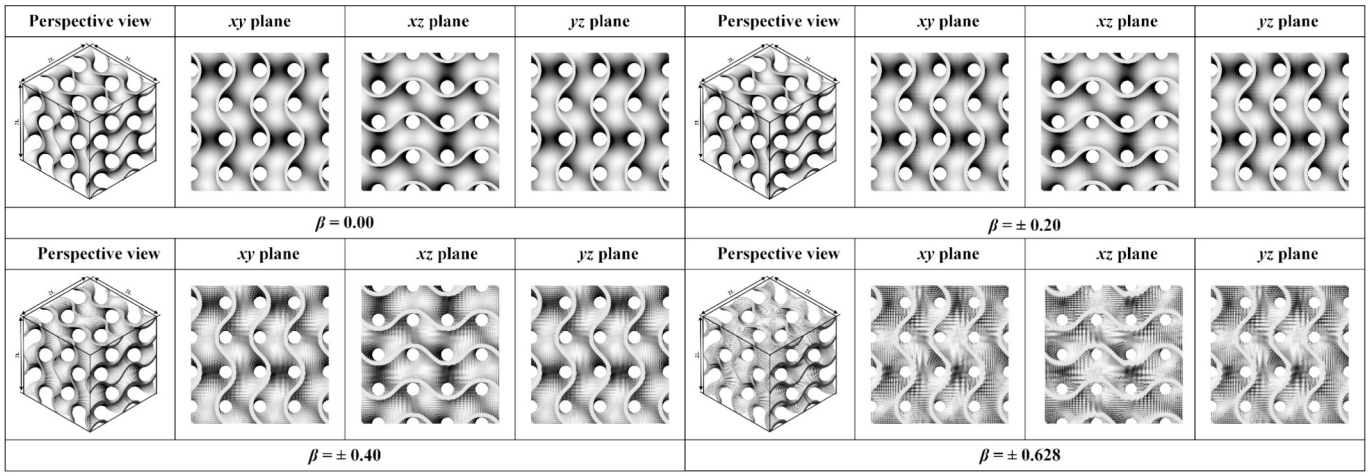

Fig. 7. Effects of different values of β on the Gyroid structure ($A(r) = \cos(\beta \cdot \sin(z^2))$).

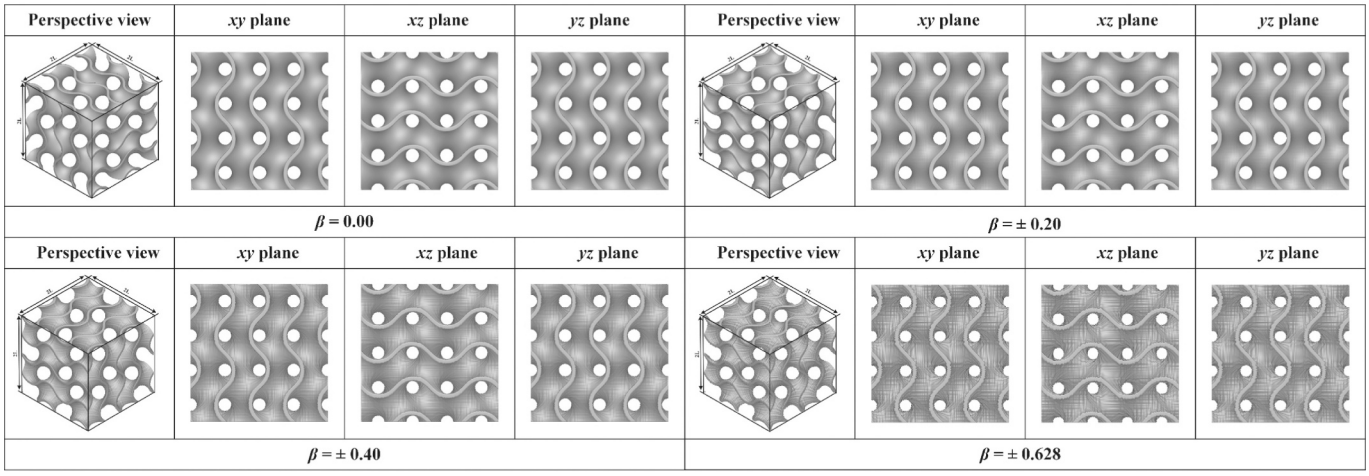

Fig. 8. Effects of different values of β on the Gyroid structure ($A(r) = \cos(\beta \cdot \sin(z^3))$).

other trigonometric function combinations (such as $\cos(\beta \cdot \sin(\cos(z^n)))$, $\sin(\beta \cdot \cos(\sin(z^n)))$, and $\sin(\beta \cdot \cos(\sin(\cos(z^n))))$ can achieve the effect of "wrinkling"; however, they will not be individually discussed here.

3.2. Periodic control

Periodic control is achieved by adjusting the periodic parameter $L(r)$ of the Gyroid function to allow the structure to exhibit varying periodic characteristics in different regions. The improved Gyroid function is expressed as follows:

$$F(r) = \cos(\frac{2\pi}{L(r)}x)\sin(\frac{2\pi}{L(r)}y) + \cos(\frac{2\pi}{L(r)}y)\sin(\frac{2\pi}{L(r)}z) + \cos(\frac{2\pi}{L(r)}z)\sin(\frac{2\pi}{L(r)}x) \tag{7}$$

Based on the corresponding mathematical derivations, $L(r)$ must remain constant (see Appendix A: Periodic control for the detailed proof). When $L(r)$ is a constant, the variation in the Gyroid structure with different L values are as shown in Fig. 9. As L decreased, the pores of the Gyroid structure contracted gradually. This behavior is attributed to a decrease in the L value, which reduced the period of the Gyroid function. Consequently, the size of the Gyroid unit decreased, which increased the number of Gyroid structural units per unit volume, thus rendering the overall structure more compact.

3.3. Phase control

Phase control is achieved by adjusting the phase parameters of the Gyroid function, thus enabling variations in the local morphology of the structure across different regions. The improved Gyroid function is mathematically expressed as follows:

$$\begin{aligned} F(r) = {} & \cos(\frac{2\pi}{L}x + \varphi_1(r))\sin(\frac{2\pi}{L}y + \varphi_2(r)) + \\ & \cos(\frac{2\pi}{L}y + \varphi_2(r))\sin(\frac{2\pi}{L}z + \varphi_3(r)) + \\ & \cos(\frac{2\pi}{L}z + \varphi_3(r))\sin(\frac{2\pi}{L}x + \varphi_1(r)) \end{aligned} \tag{8}$$

where the phase distribution functions $\varphi_i(r)$ ($i = 1,2,3$) govern the phase distribution of the Gyroid structure along the x-, y-, and z-directions, respectively.

When $\varphi_i(r)$ is a constant φ, the overall morphology of the Gyroid structure remains fundamentally unaltered. It undergoes merely a translation in three-dimensional space, with a displacement expressed as ($2\pi\varphi_1$/L, $2\pi\varphi_2$/L, $2\pi\varphi_3$/L). The spatial distribution of the Gyroid structure under different phase values φ are shown in Fig. 10. As shown, despite the visual differences exhibited by the Gyroid structure under different φ values, these differences predominantly originated from the spatial shift induced by the phase change. This translation resulted in the selected structural region not being within the complete periodic cycle.

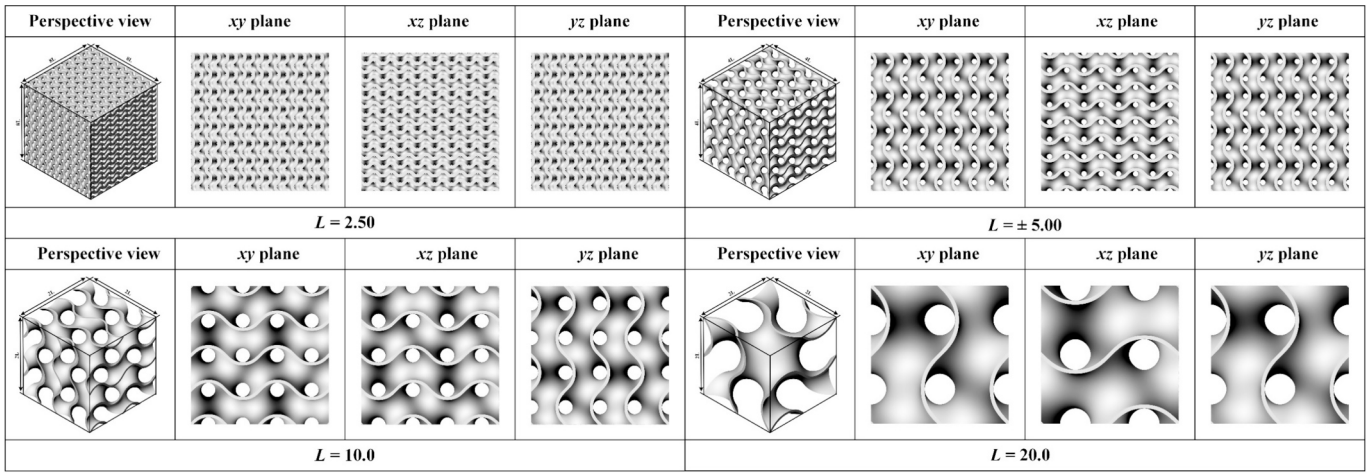

Fig. 9. Variation in the Gyroid structure with different L values.

Nevertheless, owing to the periodicity of the Gyroid structure, when φ equals $k\pi$ (k is an integer), the resulting displacement corresponded precisely to an integer multiple of $L/2$, thereby causing the Gyroid structure to be unchanged.

When $\varphi_i(r)$ is non-constant, the phase undergoes nonlinear variations, thus resulting in "compression" or "stretching" in certain regions of the Gyroid surface. However, to maintain the inherent frequency of the Gyroid function, the following conditions must be satisfied:

$$\frac{d(\frac{2\pi}{L}x+\varphi_1(r))}{dx}=\frac{d(\frac{2\pi}{L}x)}{dx}=\frac{2\pi}{L};\ \frac{d(\frac{2\pi}{L}y+\varphi_2(r))}{dy}=\frac{d(\frac{2\pi}{L}y)}{dy}=\frac{2\pi}{L};\ \frac{d(\frac{2\pi}{L}z+\varphi_3(r))}{dz}=\frac{d(\frac{2\pi}{L}z)}{dz}=\frac{2\pi}{L}; \tag{9}$$

Based on these constraints, φ_1(r) is governed by only the y- and z-directions, i.e., $\varphi_1(r) = \varphi_1(y,z)$; $\varphi_2(r)$ is governed by only the x and z directions, i.e., $\varphi_2(r) = \varphi_2(x,z)$; and $\varphi_3(r)$ is governed by only the x- and y-directions, i.e., φ_3(r) = $\varphi_3(x,y)$. To maintain the structural characteristics of the standard Gyroid function, the phase functions $\varphi_1(y,z)$, $\varphi_2(x,z)$, and $\varphi_3(x,y)$ should be composed of trigonometric functions. To achieve precise control over the morphological features of the Gyroid structure, a control factor α is introduced to form control terms. Considering $\varphi_1(y,z)$ as an example, its possible forms include:$\alpha\cdot\sin(y)$, $\alpha\cdot\sin(z)$, $\alpha\cdot\cos(y)$, $\alpha\cdot\cos(z)$, $\alpha\cdot\sin(y)\sin(z)$, $\alpha\cdot\sin(y)\cos(z)$, $\alpha\cdot\cos(y)\sin(z)$, and $\alpha\cdot\cos(y)\cos(z)$. Higher-order nested trigonometric functions are not considered for the control terms in this study because introducing high-order nonlinear terms may disrupt the intrinsic characteristics of Gyroid structure. The morphological changes in the Gyroid structure under different values of α are shown in Fig. 11.

As shown in Fig. 11, the control terms $\alpha\cdot\sin(z)$, $\alpha\cdot\cos(y)$, and $\alpha\cdot\sin(y)\cos(z)$ effectively closed the pores of the Gyroid structure. Among them, $\alpha\cdot\cos(y)$ and $\alpha\cdot\sin(y)\cos(z)$ effectively preserved the inherent characteristics of the standard Gyroid structure.

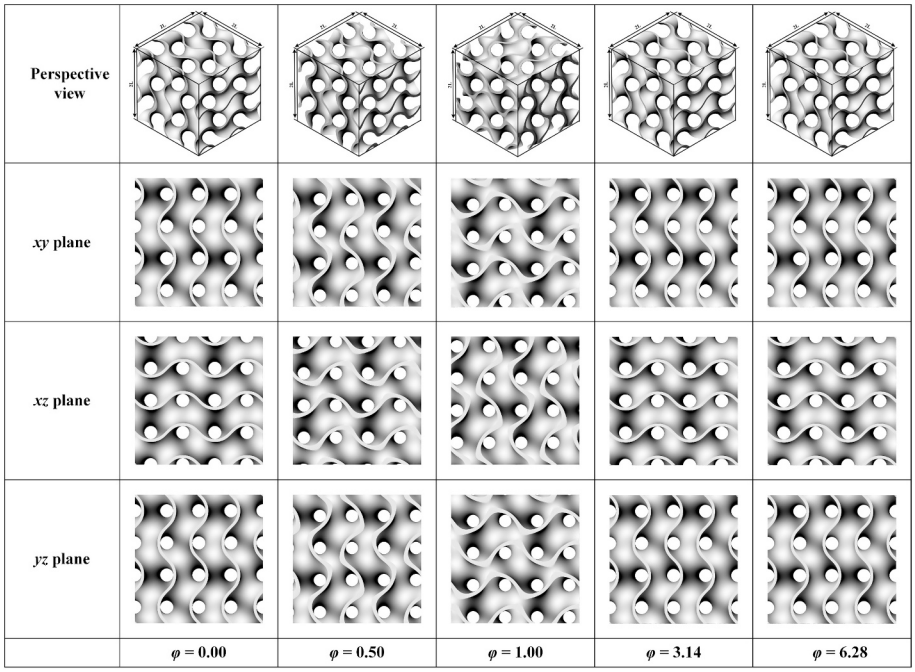

Fig. 10. Spatial distribution of the Gyroid structure under different phase values φ.

When $\varphi_1(y,z) = \alpha \cdot \sin(y)\cos(z)$, the range of α is constrained to $0.00 < \alpha < 0.80$, and the effects of α on the Gyroid structure are shown in Fig. 12. The improved Gyroid function is expressed as follows:

$$F(r) = \cos(\frac{2\pi}{L}x + \alpha\cdot\sin(\frac{2\pi}{L}y)\cos(\frac{2\pi}{L}z))\sin(\frac{2\pi}{L}y + \alpha\cdot\sin(\frac{2\pi}{L}z)\cos(\frac{2\pi}{L}x)) + \cos(\frac{2\pi}{L}y + \alpha\cdot\sin(\frac{2\pi}{L}z)\cos(\frac{2\pi}{L}x))\sin(\frac{2\pi}{L}z + \alpha\cdot\sin(\frac{2\pi}{L}x)\cos(\frac{2\pi}{L}y)) + \cos(\frac{2\pi}{L}z + \alpha\cdot\sin(\frac{2\pi}{L}x)\cos(\frac{2\pi}{L}y))\sin(\frac{2\pi}{L}x + \alpha\cdot\sin(\frac{2\pi}{L}y)\cos(\frac{2\pi}{L}z)) \tag{10}$$

Based on the amplitude control analysis, the three constituent components of the Gyroid function, namely $\cos(x)\sin(y)$, $\cos(y)\sin(z)$, and $\cos(z)\sin(x)$, regulated the size and shape of the pores in the *xy*-, *yz*-, and *xz*-planes, respectively. Considering the control term $\alpha\cdot\sin(y)\cos(z)$ as an example, its effect on the porosity of the Gyroid structure in the *xy* plane are shown in Fig. 13. As shown, adding a control term to $\cos(x)$ results in a "stretching" effect in the *x*-direction, while adding a control term to $\sin(y)$ results in a "compression" effect in the *y*-direction. The closure of the Gyroid structure's pores is primarily attributed to the "compression" effect along the *y*-direction.

The analysis above primarily focuses on the case where $\varphi_i(r)$ is a linear trigonometric function, which aim to precisely regulate the pore size and shape of the Gyroid structure. To further precisely control the structural morphology of the Gyroid function, subsequent research will explore $\varphi_i(r)$ in the form of higher-power trigonometric functions ($\beta\cdot\sin(y^n)\cos(z^n)$ as an example), such as $\beta\cdot\sin(y^2)\cos(z^2)$, $\beta\cdot\sin(y^3)\cos(z^3)$, $\beta\cdot\sin(y^4)\cos(z^4)$, among others.

(a) When $\varphi_1(y,z) = \beta\cdot\sin(y^2)\cos(z^2)$, the improved Gyroid function is expressed as follows:

$$F(r) = \cos(\frac{2\pi}{L}x + \beta\cdot\sin(\frac{2\pi}{L}y^2)\cos(\frac{2\pi}{L}z^2))\sin(\frac{2\pi}{L}y + \beta\cdot\sin(\frac{2\pi}{L}z^2)\cos(\frac{2\pi}{L}x^2)) + \cos(\frac{2\pi}{L}y + \beta\cdot\sin(\frac{2\pi}{L}z^2)\cos(\frac{2\pi}{L}x^2))\sin(\frac{2\pi}{L}z + \beta\cdot\sin(\frac{2\pi}{L}x^2)\cos(\frac{2\pi}{L}y^2)) + \cos(\frac{2\pi}{L}z + \beta\cdot\sin(\frac{2\pi}{L}x^2)\cos(\frac{2\pi}{L}y^2))\sin(\frac{2\pi}{L}x + \beta\cdot\sin(\frac{2\pi}{L}y^2)\cos(\frac{2\pi}{L}z^2)) \tag{11}$$

To maintain the structural characteristics of the standard Gyroid function, the range of β was set to $-0.15 \le \beta \le 0.15$, and the effects of β on the Gyroid structure are shown in Fig. 14.

(b) When $\varphi_1(y,z) = \beta\cdot\sin(y^3)\cos(z^3)$, the range of β is set to $-0.09 \le \beta \le 0.09$, and the effects of β on the Gyroid structure are shown in Fig. 15.

As shown in Figs. 14 and 15, the high-power trigonometric functions formed distinct concave-convex "wrinkles" on the surface of the Gyroid structure. This "wrinkle" configuration substantially augmented the surface area available for heat exchange, thereby increasing the heat exchange efficiency. Moreover, as the exponent n increased, the effect of the parameter β on the Gyroid structure exhibited a behavior analogous to that of quadratic trigonometric functions without showing a pronounced variation trend. In this study, the function $\varphi_1(y,z) = \beta\cdot\sin(y^3)\cos(z^3)$ was selected as an illustrative example for analysis. In practice, other trigonometric functions, such as $\beta\cdot\sin(z^n)$ and $\beta\cdot\cos(y^n)$, can producing the "wrinkle" effect; however, they will not be discussed individually here.

Both amplitude control and phase control can close the "through-holes" and generate surface "wrinkles" on the Gyroid structure, and these morphological transformations contribute to enhancing its heat transfer performance. Although the amplitude and phase control terms adopt different mathematical forms, the resulting through-hole-closing and wrinkle-forming morphologies are highly consistent. Considering that the control equations for amplitude control are simpler, we

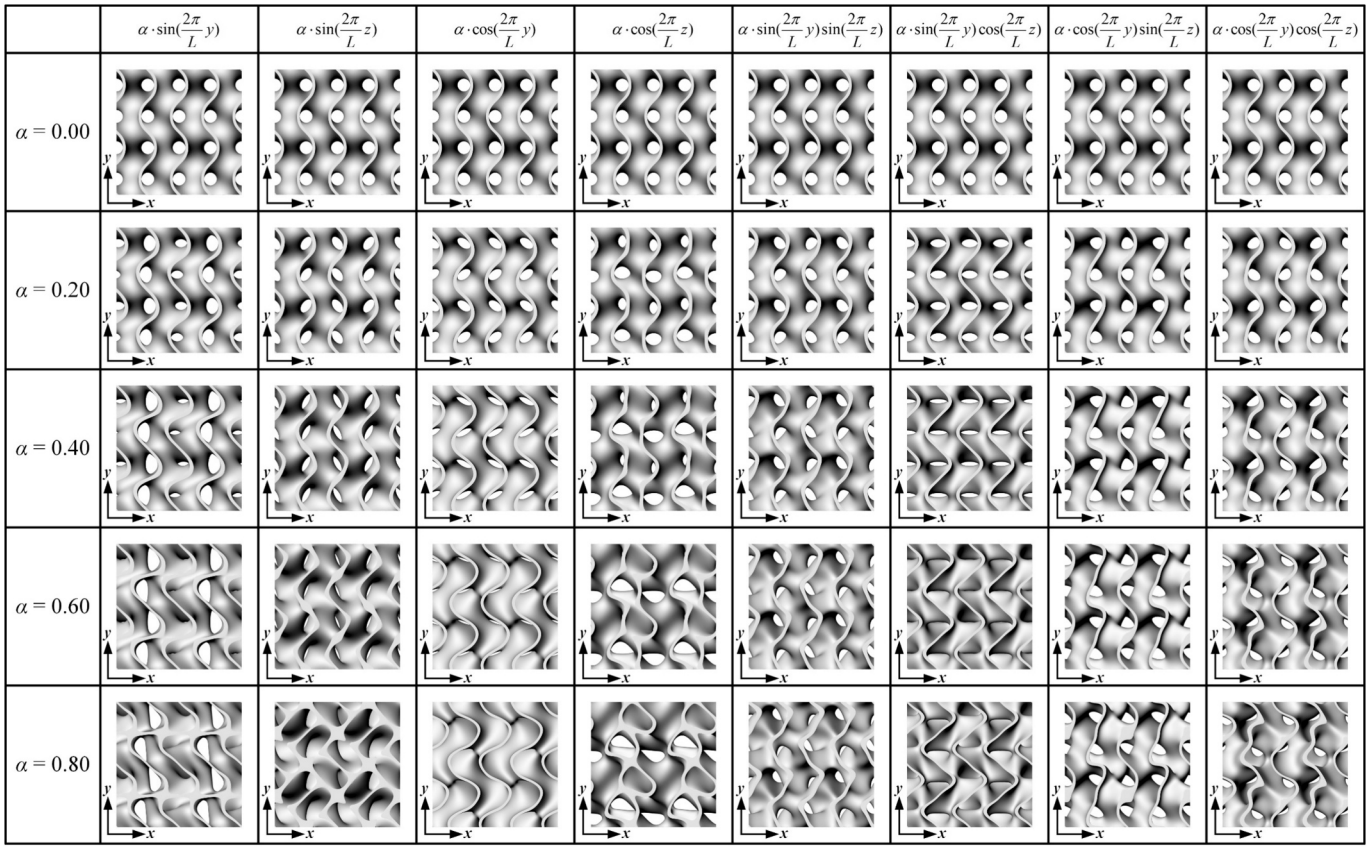

Fig. 11. The morphological changes of the Gyroid structure under different values of α.

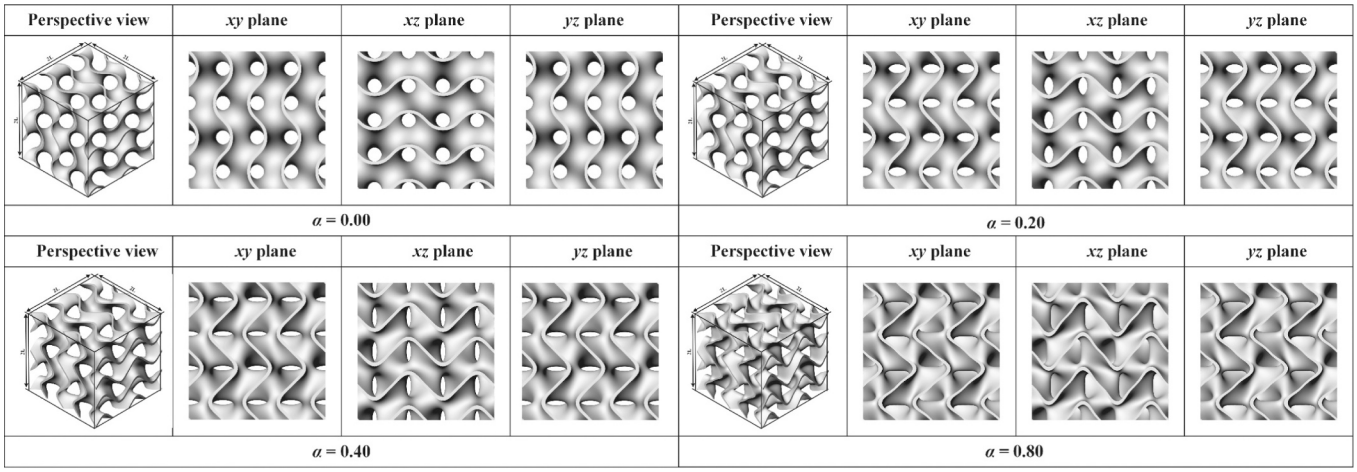

Fig. 12. Effects of different α values on the Gyroid structure ($\varphi_1(y,z) = \alpha \cdot \sin(y)\cos(z)$).

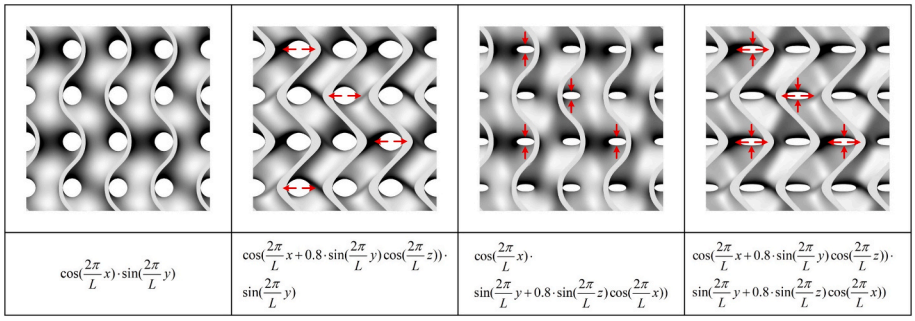

Fig. 13. Effects of $\alpha \cdot \sin(y)\cos(z)$ on the porosity of the Gyroid structure in the xy plane.

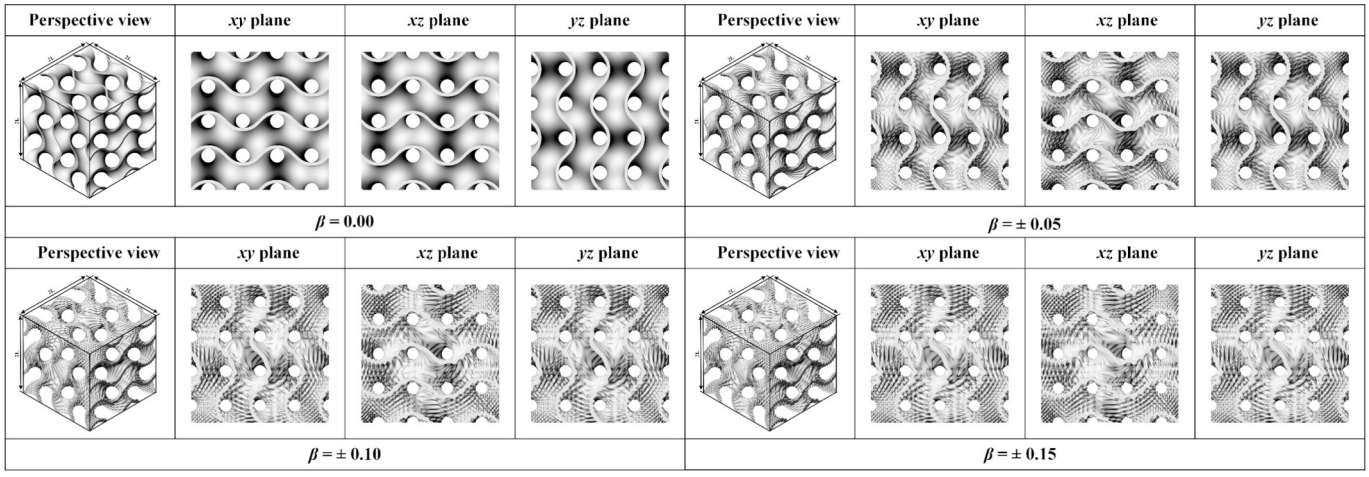

Fig. 14. Effects of different β values on the Gyroid structure ($\varphi_1(y,z) = \beta \cdot \sin(y^2)\cos(z^2)$).

recommend adopting amplitude control to induce through-hole closure and surface wrinkling. Taking $\cos(\alpha \cdot \sin(z))$ and $\cos(\beta \cdot \sin(z^2))$ as examples, the parameter α serves as the through-hole control factor, regulating the size of the through-holes, whereas β acts as the wrinkle control factor, determining the scale of the surface wrinkles. The ranges of α and β are -1.57 to 1.57 and -0.628 to 0.628, respectively. The effects of α and β on the Gyroid structure are shown in Fig. 16, and the improved Gyroid function is expressed as follows:

$$\begin{aligned} F(r) = {} & \cos(\tfrac{2\pi}{L}x)\sin(\tfrac{2\pi}{L}y)\cos(\alpha \cdot \sin(\tfrac{2\pi}{L}z))\cos(\beta \cdot \sin(\tfrac{2\pi}{L}z^2)) + \\ & \cos(\tfrac{2\pi}{L}y)\sin(\tfrac{2\pi}{L}z)\cos(\alpha \cdot \sin(\tfrac{2\pi}{L}x))\cos(\beta \cdot \sin(\tfrac{2\pi}{L}x^2)) + \\ & \cos(\tfrac{2\pi}{L}z)\sin(\tfrac{2\pi}{L}x)\cos(\alpha \cdot \sin(\tfrac{2\pi}{L}y))\cos(\beta \cdot \sin(\tfrac{2\pi}{L}y^2)) \end{aligned} \tag{12}$$

The ranges selected for the parameters (such as α and β) were determined to ensure that the characteristic features of the standard Gyroid function are preserved without damaging its intrinsic topological structure and connectivity. It should be noted that the ranges of α and β are not strict limitations, and—as clearly stated in the manuscript—this

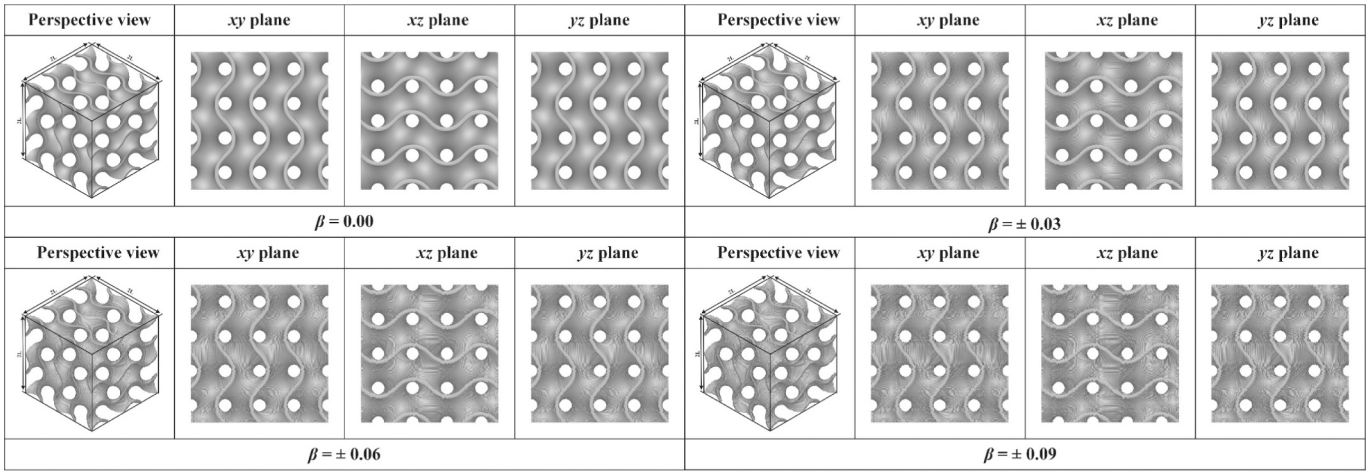

Fig. 15. Effects of different β values on the Gyroid structure ($\varphi_1(y,z) = \beta \cdot \sin(y^3)\cos(z^3)$).

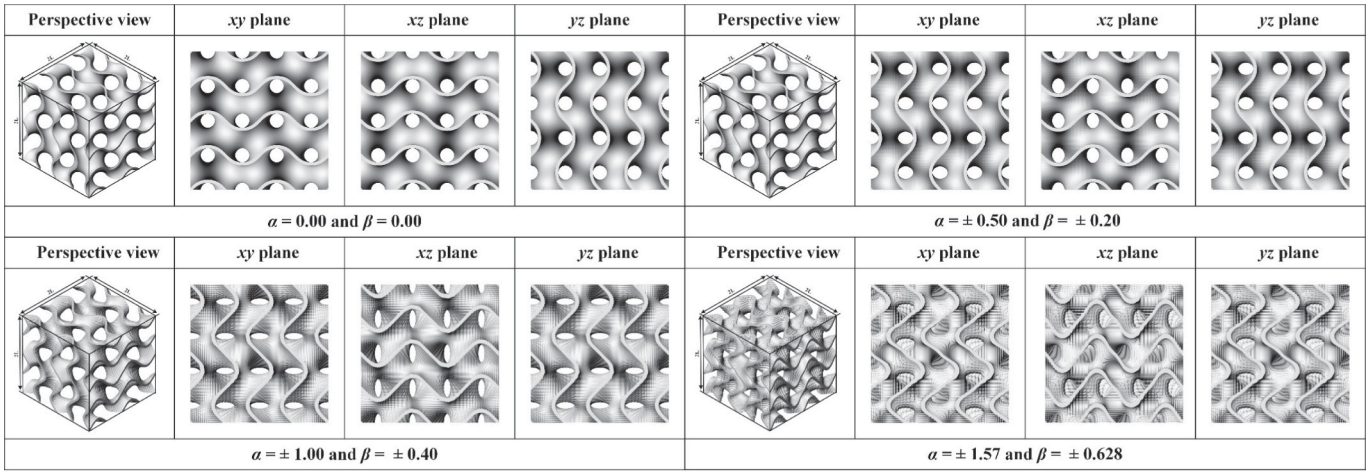

Fig. 16. Effects of different values of α and β on the Gyroid structure.

range serves as an approximate reference instead of a strict boundary condition. When the values of α and β extend far beyond the recommended ranges, two adverse consequences may occur: (1) the inherent topology and connectivity of the Gyroid structure can be severely disrupted, leading to the loss of its characteristic TPMS features; and (2) the resulting geometry may become non-manufacturable using practical additive manufacturing techniques, due to excessive distortion, self-intersections, or unsupported thin features.

4. Numerical simulation analysis

4.1. Geometric model and grid independency analysis

A 4 × 1 × 1 unit Gyroid structure is selected for analysis. To reduce inlet and outlet effects, 40 mm smooth channels are added at both ends, as shown in Fig. 17. The heating region is located on the bottom surface of the Gyroid structure, with a length of 40 mm and a width of 10 mm, using a uniform heat flux density of 400 W/cm^2 for heating. The inlet and outlet side lengths were set to 10 mm, with an inlet volumetric flow rate of 0.36 m^3/h.

Based on the conclusion of Ref. (Kus et al., 2024), the *SST k-ω* model yield results much closer to the experimental data than other turbulence model. Therefore, the CFD software was used as the solver, with the *SST k-ω* model and second-order upwind scheme applied for momentum and energy discretization. Therefore, ANSYS Fluent (academic version) was used as the CFD solver, in which the *SST k-ω* model and a second-order upwind discretization scheme were applied for both momentum and energy equations. A CFD–CHT coupled model was adopted to simultaneously resolve the fluid flow and heat conduction within the solid Gyroid structure. A uniform velocity inlet was specified, with pure water as the working fluid; the fluid properties were taken directly from the Fluent material library. The corresponding Reynolds number ranged approximately from 1300 to 8500, depending on the inlet velocity. A pressure outlet was applied at the channel exit, while the lateral walls of the channel were treated as no-slip walls. Thermally, the lateral walls were set as adiabatic surfaces, the inlet temperature was prescribed as a constant value (293 K), and a convective outflow (zero-gradient)

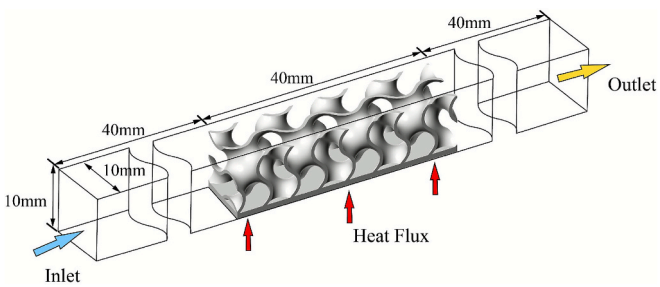

Fig. 17. Geometric model and boundary conditions of the Gyroid structure.

condition was applied at the outlet. The coupled algorithm was employed for pressure–velocity coupling, and the residual convergence criterion for the energy equation was set to 10^{-6}, ensuring numerical stability and solution accuracy. The solid material was modeled as pure copper, with properties measured from the additively manufactured samples used in this study (density: 8.92 kg/m^3, specific heat: 380 J/(kg·K), thermal conductivity: 398 W/(m·K)).

Ten different grid structures were generated to calculate the peak temperature of heating surface (T_{max}) and pressure drop between the inlet and outlet of the standard Gyroid structure (Δp). Using the maximum grid as the reference, the relative errors of T_{max} and Δp were evaluated for each grid level. The corresponding grid numbers and numerical results are presented in Fig. 18.

When the grid number reaches 1,783,556, the variations in both T_{max} and Δp become negligible. Therefore, this grid was chosen for subsequent simulations to balance accuracy and computational efficiency.

The grid details of the standard Gyroid model shown in Fig. 19. The near-wall region was refined by generating five layers of thermal boundary-layer grids, with the first layer thickness set to 0.01 mm and a growth rate of 1.2, ensuring adequate grid refinement to accurately compute the velocity and thermal boundary layers at the fluid–solid interface. The orthogonality quality factor and the average aspect ratio of the grid were 0.926 and 3.544, respectively—values closer to 1 indicate better grid quality. Additionally, the average skewness was 0.067, with lower values indicating higher grid quality.

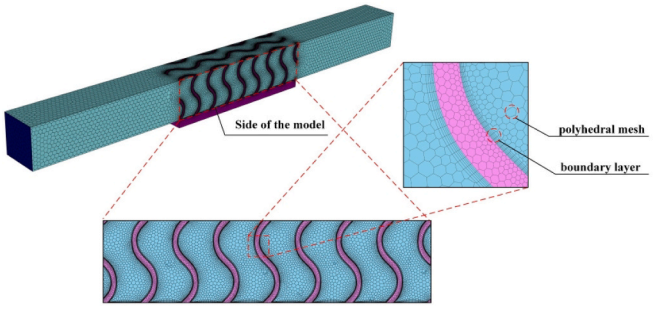

Fig. 19. The grid details of the standard Gyroid structure model.

4.2. Comparison of experimental and numerical simulation results

This paper takes Eq. (11) as the research object, and the effects of different values of α and β on the flow and heat transfer characteristics were numerically calculated. An experimental method was employed to validate the accuracy of numerical simulation results. The detailed configuration of the experimental setup, including the fabrication equipment, printing parameters, and measurement system, is provided in Appendix B: Experimental setup.

The comparison between experimental measurements and numerical simulations of Δp and T_{max} for the three Gyroid structures across various flow rates are shown in Fig. 20. In Case 1, corresponding to the standard Gyroid structure ($\alpha = 0.00$, $\beta = 0.00$), the maximum deviations in Δp and T_{max} were 4.91 % and 1.20 %, respectively. In Case 2, representing the Gyroid structure with completely closed "through-holes" ($\alpha = 1.57$, $\beta = 0.00$), the maximum deviations were 4.75 % for Δp and 0.87 % for T_{max}. In Case 3, representing the Gyroid structure with surface "wrinkles" ($\alpha = 0.00$, $\beta = 0.628$), the corresponding maximum deviations were 7.19 % and 0.98 %. Overall, the experimental data exhibited excellent consistency with the numerical simulations, with deviations in both pressure drop and temperature maintained within acceptable limits, thereby satisfying the accuracy requirements for heat transfer experiments.

4.3. The effect of α and β on the flow and heat transfer characteristics

The velocity magnitude contours and streamlines at the $x = 0$ cross-sections for different α and β values are shown in Fig. 21. When $\alpha = 0.00$, the velocity distribution inside the Gyroid channel is relatively uniform, with well-organized streamlines and only a few vortical structures. However, as α increases, the "through-holes" within the Gyroid structure progressively close, forcing the fluid to flow along more tortuous paths. This causes the velocity field to become markedly non-uniform. In particular, at $\alpha = 1.57$, numerous alternating high- and low-velocity regions appear, accompanied by the formation of small-scale vortices and secondary flows (as highlighted by the black circles), indicating significantly enhanced flow disturbances and mixing. These enhanced flow disturbances strengthen fluid mixing and thereby improve convective heat transfer performance. As β increases, wrinkle-like features gradually emerge on the Gyroid surface, making the near-wall geometry more complex. The surface wrinkles intensify the local velocity gradients and disrupt the original boundary-layer structure, leading to a more pronounced alternation of high- and low-velocity regions. When $\beta \geq 0.40$, pronounced local flow disturbances and noticeable boundary-layer disruption can be observed (as indicated by the black rectangles). These wrinkle-induced perturbations enhance fluid mixing and energy exchange efficiency, thereby further improving convective heat-transfer performance.

The temperature distribution contours of the heating surface of the Gyroid structure under various α and β values are shown in Fig. 22,

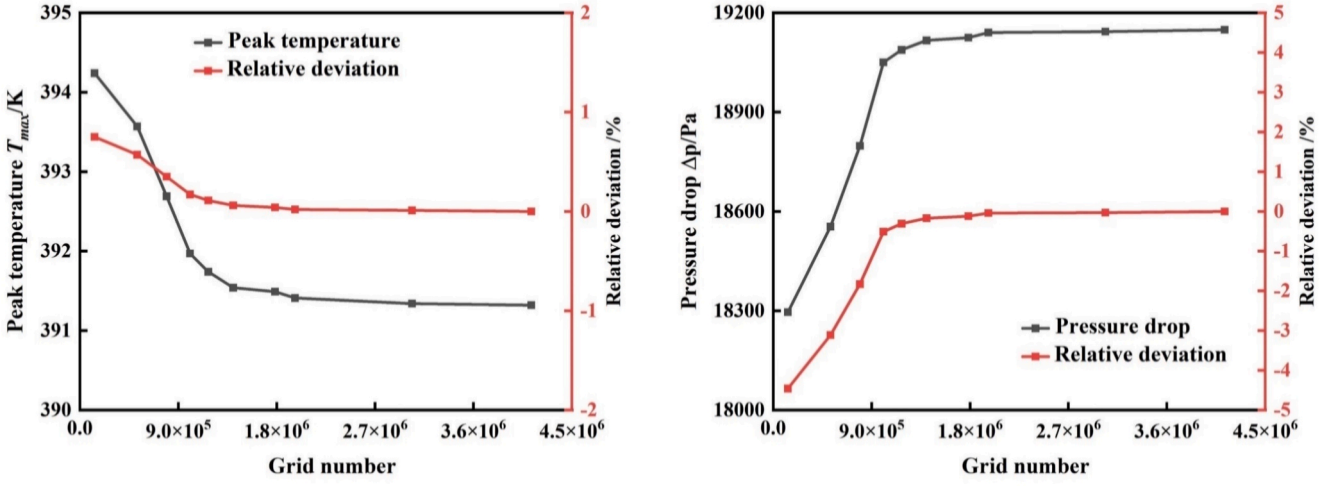

Fig. 18. Grid independence verification results.

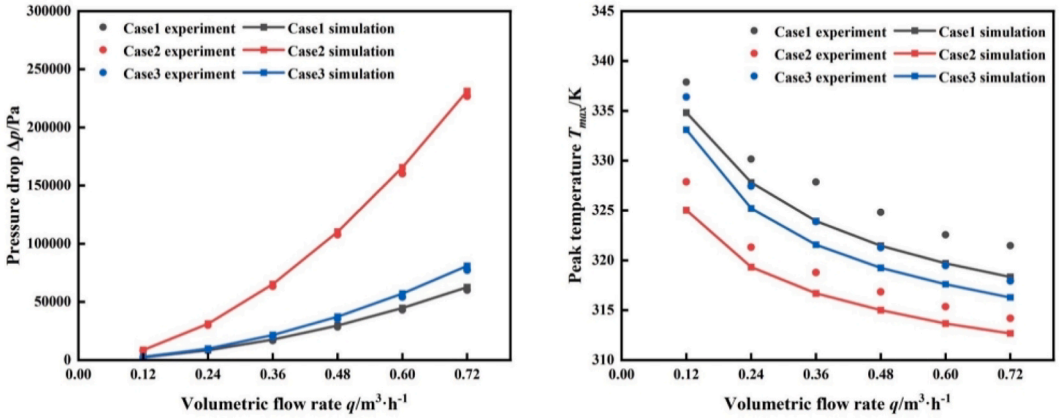

Fig. 20. Comparison between the experimental and numerical results.

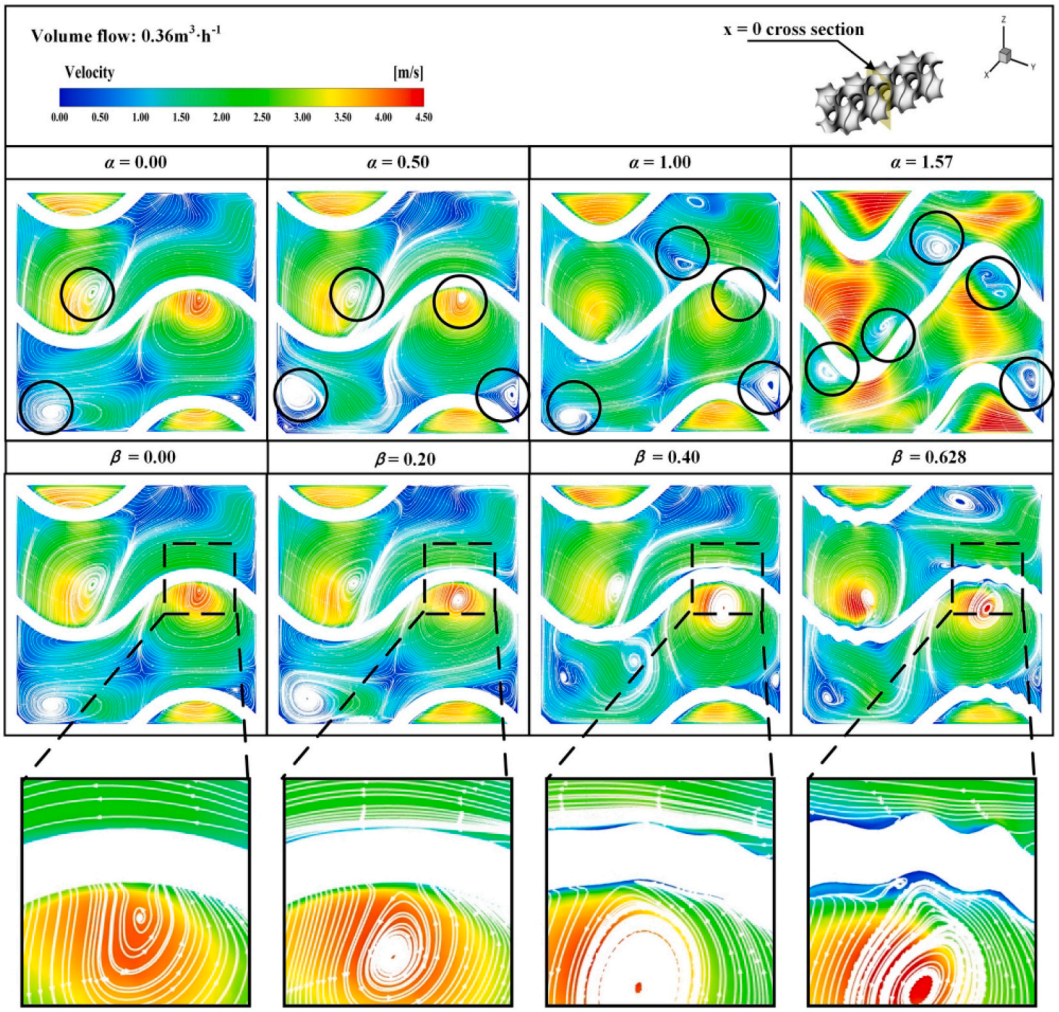

Fig. 21. Velocity distribution contours and streamlines at the $x = 0$ cross-section for different α and β values.

where the offset parameter C was set to ± 0.25 to generate the inner and outer Gyroid surfaces, corresponding to a wall thickness of 0.5 mm. It can be seen that the temperature field on the heating surface is significantly affected by variations in α and β. When $\alpha = 0.00$ or $\beta = 0.00$, a pronounced non-uniformity in the temperature field is observed, accompanied by a distinct temperature gradient, with the peak temperature reaching as high as 391.5 K. As the values of α and β increase, T_{max} is gradually reduced, and the temperature distribution becomes more uniform. Specifically, when α is increased to 1.57, T_{max} is reduced to 368.6 K, whereas when β is increased to 0.628, T_{max} is reduced to 373.8 K.

The effects of α and β on the peak temperature of heating surface (T_{max}) in the Gyroid structure are illustrated in Fig. 23. With increasing volumetric flow rate, T_{max} of Gyroid structure exhibits a linearly

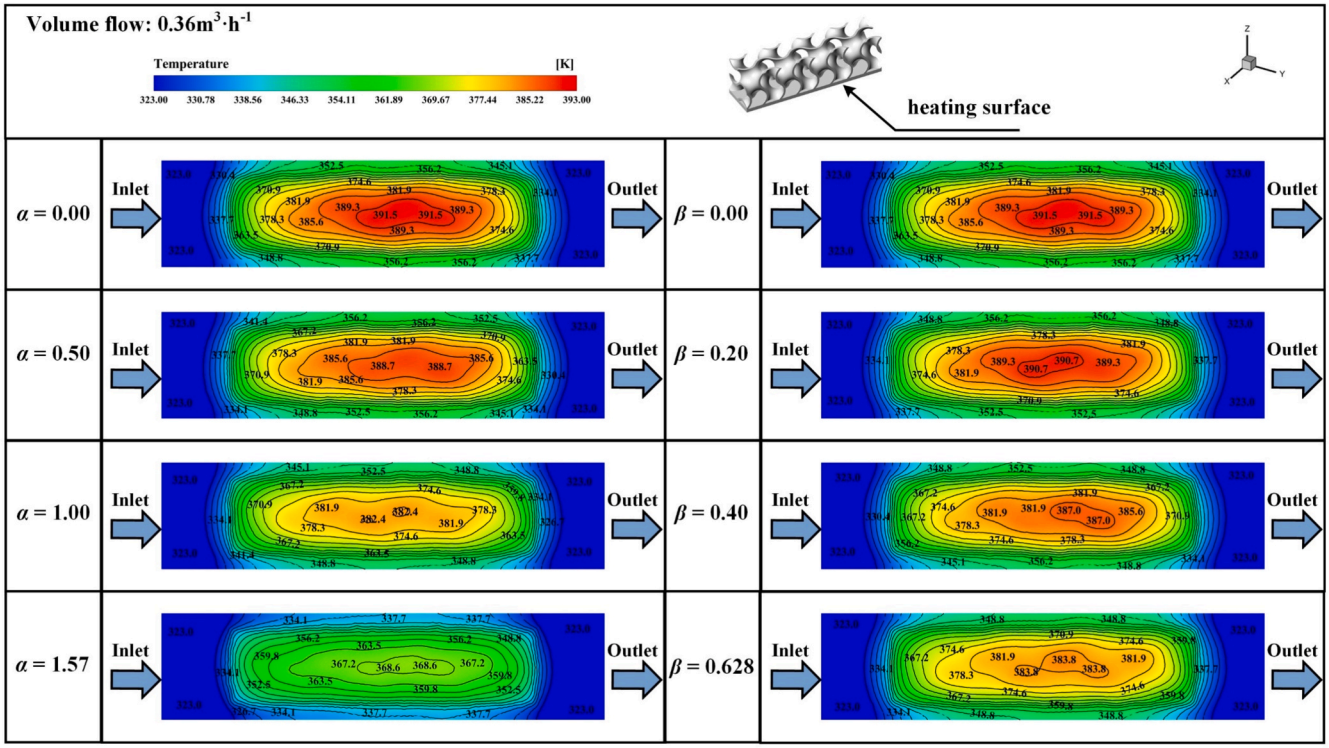

Fig. 22. Temperature distribution contour of heating surface at different α and β values.

decreasing trend. Within the volumetric flow rate range of 0.12–0.72 m^3/h, T_{max} of Gyroid structure gradually decreases with increasing α and β values. When α is increased to 1.57, T_{max} is reduced by 19.0–33.6 across the different flow rates, while an increase in β to 0.628 results in a reduction of 7.3–8.8 K across the different flow rates.

The effects of α and β on the convective heat transfer coefficient (h) of the Gyroid structure are illustrated in Fig. 24. With the increase in volumetric flow rate, h of the Gyroid structure exhibits a linear increasing trend. Within the volumetric flow rate range of 0.12–0.72 m^3/h, h gradually increases with increasing α and β values. When α is increased to 1.57, h increases by 29.4–33.7 %, while an increase in β to 0.628 results in a rise of 5.4–7.9 %.

Enhanced convective heat transfer is generally accompanied by an increase in pressure-drop losses and flow resistance. The Effect of α and β on pressure drop of Gyroid structure are shown in Fig. 25. As the flow rate increases, Δp exhibits an increasing trend, consistent with fundamental fluid dynamic principles. With increasing α, the through-holes of the Gyroid structure gradually close, forcing the fluid to flow through more tortuous, non-linear channels, thereby increasing the flow-path losses. As β increases, wrinkles form on the structure surface, enhancing near-wall shear and introducing local disturbances, which lead to higher frictional resistance and local pressure losses. Overall, the increase in α and β results in only a slight rise in pressure drop. However, when α reaches 1.57 (“through-holes” completely closed), the originally relatively continuous flow paths are completely disrupted, and the fluid is forced to travel through more tortuous and circuitous channels, leading to a significant increase in viscous dissipation and consequently a marked rise in pressure drop.

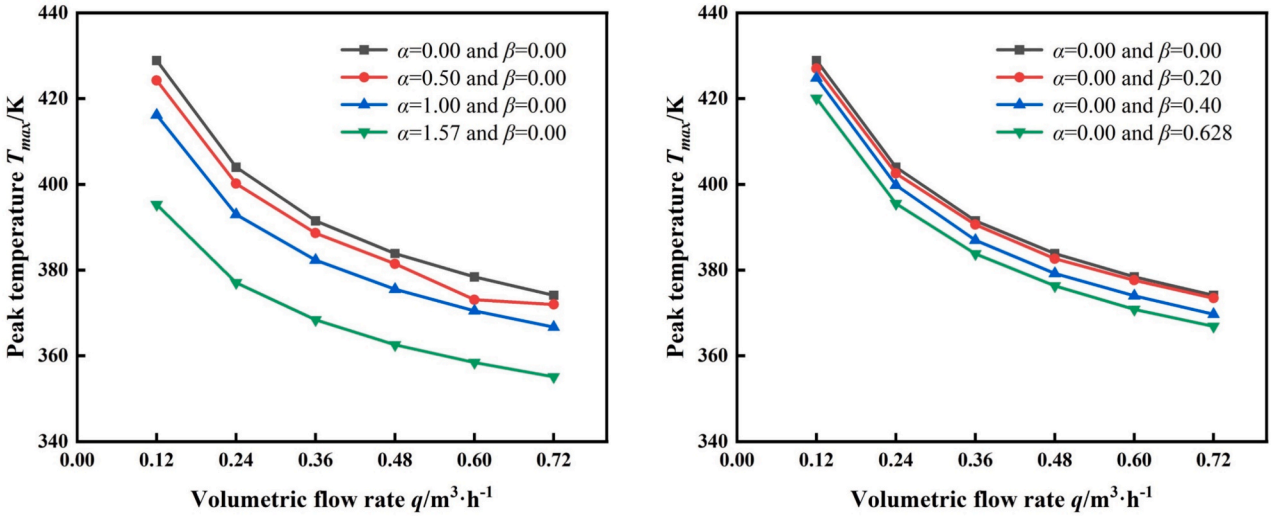

Fig. 23. Effect of α and β on the peak temperature of heating surface.

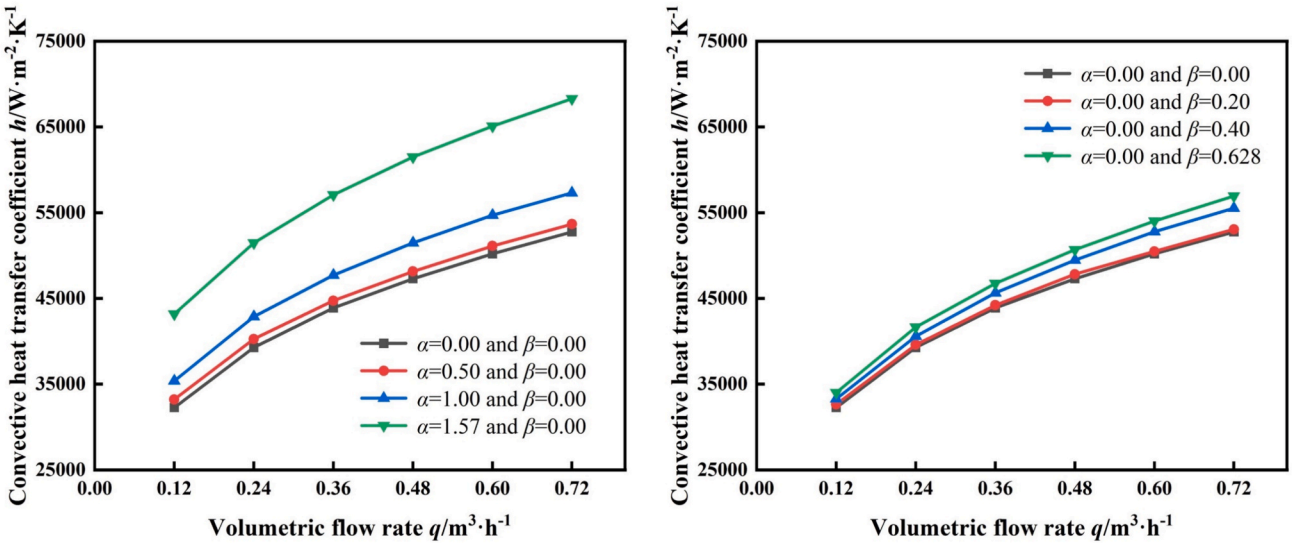

Fig. 24. Effect of α and β on convective heat transfer coefficient of Gyroid structure.

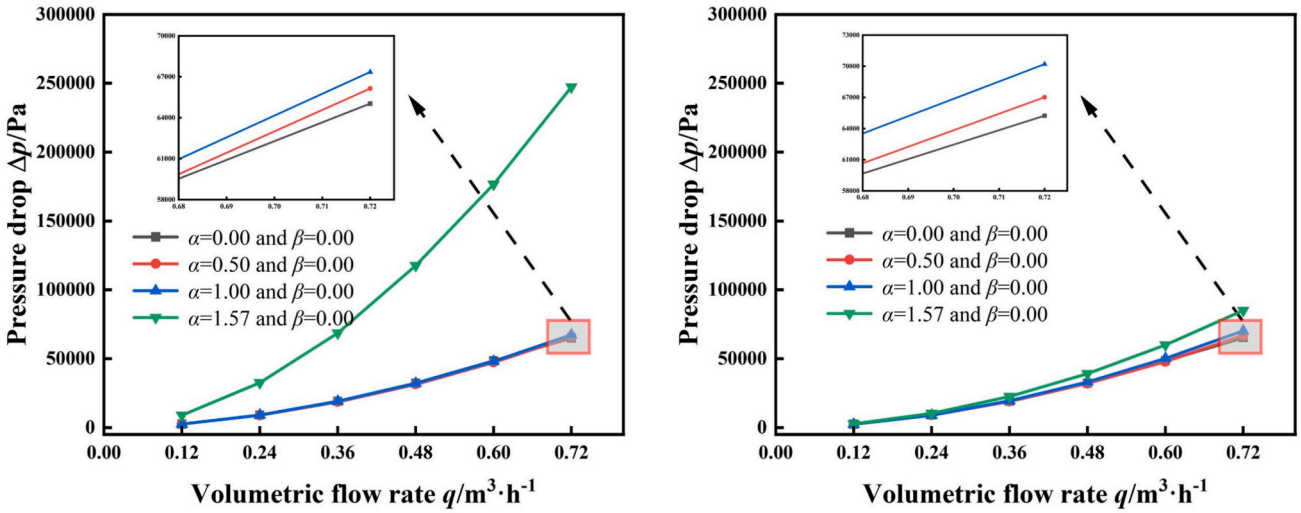

Fig. 25. Effect of α and β on pressure drop of Gyroid structure.

Although the improved Gyroid structure can significantly enhance convective heat transfer, this enhancement is generally accompanied by an increase in flow resistance. In particular, as the volumetric flow rate rises, the pressure-drop loss (Δp) increases exponentially, which leads to higher pumping-power consumption in engineering applications. Therefore, it is essential to balance heat-transfer performance and pressure-drop loss when optimizing the structure.

To quantitatively evaluate the overall heat-transfer performance of the improved Gyroid structure, the performance evaluation coefficient (*PEC*) (Liu et al., 2021) is adopted in this study, defined as:

$$PEC = \frac{h/h_0}{(\Delta p/\Delta p_0)^{1/3}} \tag{13}$$

where h and Δp represent the convective heat-transfer coefficient and pressure drop of the improved Gyroid structure, and h_0 and Δp_0 represent those of the standard Gyroid structure. When $PEC > 1$, it indicates that the improved Gyroid structure outperforms the standard structure when both heat-transfer enhancement and flow resistance are considered.

The effect of α and β on *PEC* of Gyroid structure is shown in Fig. 26.

As α and β increase, PEC exhibits a "rise-then-fall" trend, reaching its maximum at $\alpha = 0.9$ and $\beta = 0.5$, respectively. It is worth noting that although the structure achieves the highest convective heat-transfer coefficient and the lowest maximum temperature at $\alpha = 2.5$, its *PEC* is less than 1, indicating inferior overall performance compared with the standard Gyroid structure. Therefore, considering both heat-transfer enhancement and flow resistance, $\alpha = 1.20$ or $\beta = 0.628$ should be selected. Under these conditions, *PEC* exceeds 1, and the improved Gyroid structure achieves both a higher convective heat-transfer coefficient and a lower peak temperature.

With the increase of α, the "through-holes" in the Gyroid structure are gradually closed, forcing the fluid to be directed into the non-linear flow channels formed by the complex surfaces of the Gyroid, thereby enhancing the disruption of the boundary layer, generating more secondary flows and vortices, and thus improving the convective heat transfer performance. Unlike the mechanism in which increasing α leads to the closure of "through-holes," the increase of β primarily enhances heat transfer performance by altering the geometric characteristics of the structural surface. With the increase of β, "wrinkles" gradually form on the Gyroid surface, which not only increase the heat transfer area but also destabilize the fluid boundary layer, generating strong secondary

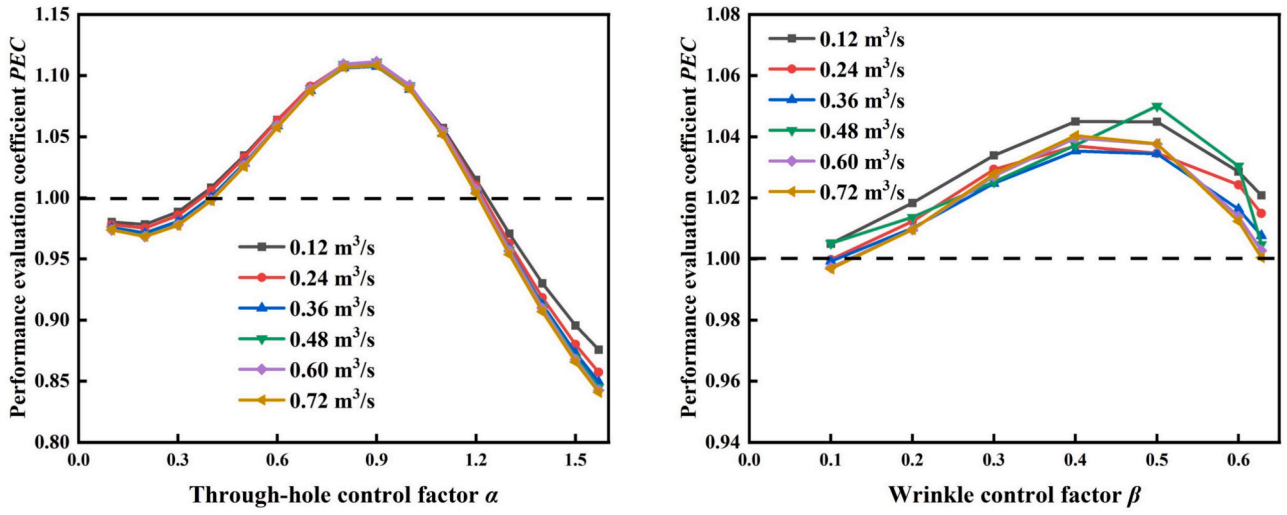

Fig. 26. Effect of α and β on performance evaluation coefficient of Gyroid structure.

flows and turbulence, thereby improving the convective heat transfer performance.

5. Conclusion

In this study, the Gyroid-type TPMS structure was selected as the research object, and three functional improvement methods—amplitude control, periodicity control, and phase control—were proposed. The effects of different control strategies on the morphological characteristics of the Gyroid structure were analyzed comprehensively, and the flow and heat transfer characteristics of the improved Gyroid structure were analyzed numerically and experimentally. The main conclusions of this study are summarized as follows:

(1) When the amplitude control term $A(r)$ and the phase control term $\varphi_i(r)$ are linear trigonometric functions, both amplitude and phase control can precisely regulate the surface morphology and internal "through-hole" size of the Gyroid structure.
(2) When the amplitude control term $A(r)$ and the phase control term $\varphi_i(r)$ are expressed as higher-order trigonometric functions, both amplitude and phase control can induce distinct "wrinkle" features on the surface of the Gyroid structure.
(3) Both the closure of "through-holes" and the formation of surface "wrinkles" in the Gyroid structure can enhance its heat transfer performance. Within the volumetric flow rate range of 0.12–0.72 m^3/h, as α increases, T_{max} of the Gyroid structure decreases by 19.0–33.6 K, while h increases by 29.4–33.7 %. Similarly, as β increases, T_{max} decreases by 7.3–8.8 K, and h increases by 5.4–7.9 %.
(4) Considering both heat-transfer enhancement and flow resistance, $\alpha = 1.20$ or $\beta = 0.628$ should be selected. Under these conditions, the *PEC* exceeds 1, and the improved Gyroid structure achieves a higher convective heat-transfer coefficient along with a lower maximum temperature.

CRediT authorship contribution statement

Kaiwen Qin: Writing – review & editing, Writing – original draft, Software, Methodology, Funding acquisition, Conceptualization. **Si Yang:** Validation, Methodology, Investigation, Formal analysis. **Tingxiang Lv:** Writing – review & editing, Software, Methodology, Conceptualization. **Xijun Zhao:** Software, Methodology, Formal analysis, Conceptualization. **Xiaobin Tang:** Writing – review & editing, Writing – original draft, Project administration, Methodology, Funding acquisition, Formal analysis.

Declaration of competing interest

The authors declare that they have no known competing financial interests or personal relationships that could have appeared to influence the work reported in this paper.

Acknowledgments

This work was supported by the National Natural Science Foundation of China (Grant No. 12575362), the Graduate Research Innovation Program Project of Jiangsu Province (Grant No. KYCX24_0617).

Appendix A:. Periodic control

Periodic control is achieved by adjusting the periodic parameter $L(r)$ of the Gyroid function to allow the structure to exhibit varying periodic characteristics in different regions. The improved Gyroid function is expressed as follows:

$$F(r) = \cos(\frac{2\pi}{L(r)}x)\sin(\frac{2\pi}{L(r)}y) + \cos(\frac{2\pi}{L(r)}y)\sin(\frac{2\pi}{L(r)}z) + \cos(\frac{2\pi}{L(r)}z)\sin(\frac{2\pi}{L(r)}x) \quad (14)$$

When $L(r)$ is a constant, the Gyroid surface exhibits a period L along the x-, y-, and z-directions, with a mean curvature $H = 0$. However, when $L(r) = L(x,y,z)$ is non-constant, the Gyroid function no longer satisfies the requirements of TPMS. A triply periodic minimal surface can be defined as follows:

Definition 1 **(triply periodicity):** A surface is defined as triply periodic if three linearly independent translation vectors $p_1, p_2, p_3 \in R^3$ exist such

that all points (x,y,z) satisfying the implicit function equation $F(x,y,z) = 0$ satisfy the following conditions:

$$F(x+p_{i,x}, y+p_{i,y}, z+p_{i,z}) = F(x,y,z), i = 1,2,3 \tag{15}$$

Definition 2 **(minimal surface):** A surface is defined as minimal if its mean curvature satisfies $H = 0$. For an implicit function surface $F(x,y,z) = 0$, its mean curvature is expressed as follows (Fisher et al., 2022):

$$H = -\frac{1}{2|\nabla F|^3}\left[|\nabla F|^2 \Delta F - \sum_{i,j=1}^{3} F_{x_i} F_{x_j} F_{x_i x_j}\right] \tag{16}$$

where the gradient $\nabla F = (F_x, F_y, F_z)$ represents the vector composed of the first-order partial derivatives of F, the Laplacian operator $\Delta F = F_{xx} + F_{yy} + F_{zz}$ is the sum of the second-order partial derivatives of F, and F_{xixj} denotes the second-order partial derivative of F with respect to x_i and x_j.

Analysis of triply periodicity: Let $L = L(x,y,z) > 0$, which comprises trigonometric functions. Consider a translation along the x-direction: $(x,y,z) \rightarrow (x+p,y,z)$. Thus:

$$\begin{aligned} F(x+p,y,z) = &\cos\left(\frac{2\pi(x+p)}{L(x+p,y,z)}\right)\sin\left(\frac{2\pi y}{L(x+p,y,z)}\right) + \\ &\cos\left(\frac{2\pi y}{L(x+p,y,z)}\right)\sin\left(\frac{2\pi z}{L(x+p,y,z)}\right) + \\ &\cos\left(\frac{2\pi z}{L(x+p,y,z)}\right)\sin\left(\frac{2\pi(x+p)}{L(x+p,y,z)}\right) \end{aligned} \tag{17}$$

To satisfy triple periodicity, $F(x+p,y,z) = F(x,y,z)$ must hold for all (x,y,z). This requires:

$$\frac{2\pi(x+p)}{L(x,y,z)} = \frac{2\pi x}{L(x,y,z)} + 2k\pi, k = 1,2,3\ldots \tag{18}$$

Solving this equation yields $p = k \cdot L(x,y,z)$. As p and k are constants, $L(x,y,z)$ must be a constant as well.

Analysis of minimal surface: We define $u = 2\pi x/L(x,y,z)$, $v = 2\pi y/L(x,y,z)$, $w = 2\pi z/L(x,y,z)$. Therefore, the gradient of $F(x,y,z)$ is expressed as follows:

$$\nabla F = \frac{2\pi}{L(x,y,z)}\begin{pmatrix} A \\ B \\ C \end{pmatrix} - \frac{2\pi}{L(x,y,z)^2} G \nabla L(x,y,z) \tag{19}$$

where $A = \partial F/\partial u$, $B = \partial F/\partial v$, $C = \partial F/\partial w$, and $G = xA + yB + zC$.

The Laplacian of $F(x,y,z)$ is expressed as:

$$\begin{aligned} \Delta F = &\frac{\partial}{\partial x}\left(\frac{2\pi}{L(x,y,z)}A - \frac{2\pi}{L(x,y,z)^2}\frac{\partial L}{\partial x}G\right) + \\ &\frac{\partial}{\partial y}\left(\frac{2\pi}{L(x,y,z)}B - \frac{2\pi}{L(x,y,z)^2}\frac{\partial L}{\partial y}G\right) + \\ &\frac{\partial}{\partial z}\left(\frac{2\pi}{L(x,y,z)}C - \frac{2\pi}{L(x,y,z)^2}\frac{\partial L}{\partial z}G\right) \end{aligned} \tag{20}$$

Furthermore, the term $\sum_{i,j=1}^{3} F_{x_i} F_{x_j} F_{x_i x_j}$ is expressed as:

$$\begin{aligned} &\sum_{i,j=1}^{3} F_{xi} F_{xj} F_{xixj} = F_x^2 F_{xx} + F_y^2 F_{yy} + F_z^2 F_{zz} + 2(F_x F_y F_{xy} + F_x F_z F_{xz} + F_y F_z F_{yz}) \\ &= \left(\frac{2\pi}{L(x,y,z)}\right)^3 [A^2\frac{\partial A}{\partial x} + B^2\frac{\partial B}{\partial y} + C^2\frac{\partial B}{\partial z} + 2AB\frac{\partial A}{\partial y} + 2AC\frac{\partial A}{\partial z} + 2BC\frac{\partial B}{\partial z}] - \\ &\left(\frac{2\pi}{L(x,y,z)^2}\right)^2 G[\left(\frac{\partial L}{\partial x}\right)^2\frac{\partial G}{\partial x} + \left(\frac{\partial L}{\partial y}\right)^2\frac{\partial G}{\partial y} + \left(\frac{\partial L}{\partial z}\right)^2\frac{\partial G}{\partial z}] + \textit{crossterms} \end{aligned} \tag{21}$$

To satisfy the mean curvature $H = 0$, $|\nabla F|^2 \Delta F = \sum_{i,j=1}^{3} F_{x_i} F_{x_j} F_{x_i x_j}$ must be satisfied, according to Eq. (16). By substituting Eqs. (19), (20), and (21), because of the presence of cross terms on the right side of the equation, $H = 0$ can only be satisfied when $\nabla L(x,y,z) = 0$, which implies that $L(x,y,z)$ must be a constant.

Appendix B:. Experimental setup

The experimental system, as shown in Figs. 27-29, consists of three parts: a schematic diagram of the experimental principle (Fig. 27), a photograph of the experimental system (Fig. 28), and a photograph of the experimental model (Fig. 29).

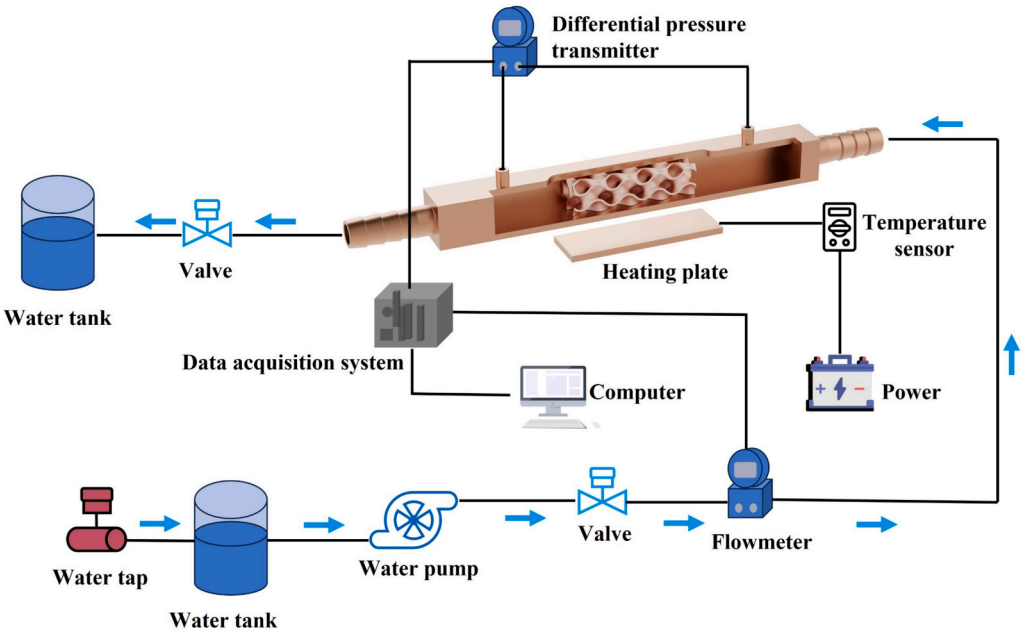

Fig. 27. Schematic of the experimental setup

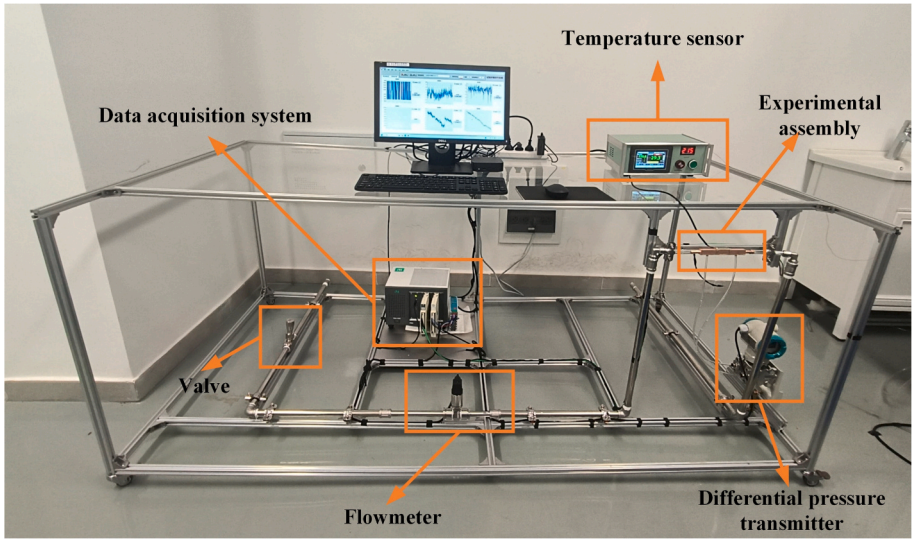

Fig. 28. Experimental system setup

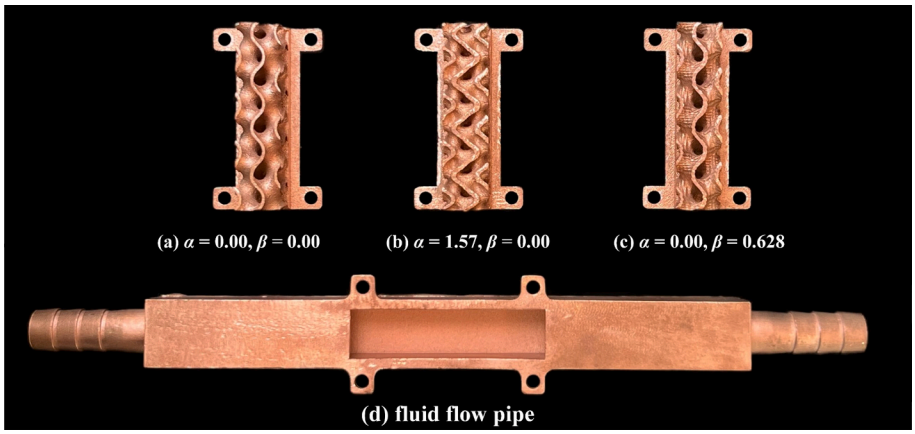

Fig. 29. 3D printed Gyroid structure

The experimental setup includes an heating plate, thermocouples, a temperature sensor, a flowmeter, a differential pressure transmitter, a data acquisition system, a water pump, and regulating valves. The heating plate (AlN), with a power of 500 W and a heat flux density of 125 W/cm^3, providing a stable heat source for the experiment. The flowmeter (Hersman type, DN10), with a range from 0 to 1.2 m^3/h, and the differential pressure transmitter (XL3051DP), with a range from 0 to 500 KPa, were used to monitor flow and pressure, respectively. The thermocouples (K-type, ASG-IN600) had a measurement range of −20 to 200 °C. The measurement accuracy of both the flowmeter and the K-type thermocouples was 1 %, while the differential pressure transmitter exhibited a precision of 0.075 %. The diameter of the flow channel piping used in the system was 10 mm.

The data acquisition (National Instruments, NI) system collected experimental data in real time. Volumetric flow rate and pressure drop were measured using the NI TB-4300C data acquisition card, while temperature data was collected with the TB-4353 thermocouple acquisition card. Flow regulation was achieved through manual valve adjustments, and data was recorded under different volumetric flow rate conditions for the four types of Gyroid structures. Experimental data was collected at 0.1-second intervals, with a total of 1000 data points collected per experiment. The average of these data points was taken to minimize random errors and ensure statistical stability and accuracy.

The Gyroid experimental model shown in Fig. 29 was fabricated using selective laser melting (SLM) technology by XiHe Additive Manufacturing Co., Ltd., employing a green-laser metal additive manufacturing system. Pure copper powder was used as the printing material. Owing to the intrinsic characteristics of LPBF processes, the as-built copper structures exhibited notable surface roughness, partly caused by partially melted powder particles adhered to the surface. To mitigate the influence of surface roughness on the heat transfer performance, the printed samples underwent post-processing, including sandblasting and mechanical polishing, to reduce the presence of adhered particles and improve the surface quality. During laser powder bed fusion, partially unmelted particles may remain adhered to the surface, which can adversely affect the heat transfer performance of the printed Gyroid structures. Following fabrication and surface treatment, the specimens were subjected to heat treatment, resulting in a thermal conductivity of 398 W/(m·K) and a density of 8.92 g/cm^3.

The maximum temperature (T_{max}) of the structure was measured using a K-type thermocouple, which was placed at the center of the heating plate to directly record the peak temperature during operation. To enhance the interfacial thermal conductance during experiments, an indium–tin alloy was applied between the heating plate and the Gyroid structure to reduce contact thermal resistance. The indium–tin alloy exhibits a thermal conductivity of 80 W/(m·K), a density of 6.89 g/cm^3, and a melting point of 60 °C.

To validate the accuracy of the numerical simulations, experiments were conducted to measure the pressure drop (Δp) and maximum temperature (T_{max}) of three types of Gyroid structures under different volumetric flow rate conditions. The experiments were carried out with a heating power of 500 W, corresponding to a heat flux density of 125 W/cm^2. The obtained results were then compared with numerical predictions under identical boundary conditions to assess the reliability of the simulations.

Data availability

Data will be made available on request.

References

Barakat, A., Sun, B.B., 2024. Enhanced convective heat transfer in new triply periodic minimal surface structures: Numerical and experimental investigation. Int. J. Heat Mass Transf. 227, 125538.
Cheng, Z., Xu, R., Jiang, P.X., 2021. Morphology, flow and heat transfer in triply periodic minimal surface based porous structures. Int. J. Heat Mass Transf. 170, 120902.
Dong, Z., Zhao, X., 2021. Application of TPMS structure in bone regeneration. Eng. Regener. 2, 154–162.
Dong, H., Zhou, F., Lu, C., et al., 2025. Upcycled coffee grounds and beeswax-derived all-bio-based PCMs for dual-function solar harvesting and thermal storage. Bioresour. Technol. 133573.
Feng, J., Fu, J., Yao, X., et al., 2022. Triply periodic minimal surface (TPMS) porous structures: From multi-scale design, precise additive manufacturing to multidisciplinary applications. Int. J. Extreme Manuf. 4 (2), 022001.
Feng, G., Li, S., Xiao, L., et al., 2023. Mechanical properties and deformation behavior of functionally graded TPMS structures under static and dynamic loading. Int. J. Impact Eng 176, 104554.
Fisher J W, Miller S W, Bartolai J, et al. 2022. Using Mean Curvature of Implicitly Defined Minimal Surface Approximations to Generate New Unit Cells for Lattice Design.
Fisher J W, Miller S W, Bartolai J, et al. 2022. Using Mean Curvature of Implicitly Defined Minimal Surface Approximations to Generate New Unit Cells for Lattice Design. In: Proceedings of the 33rd Annual International Solid Freeform Fabrication Symposium – An Additive Manufacturing Conference, Austin, TX, USA, pp. 2233–2243.
Gado, M.G., Al-Ketan, O., Aziz, M., et al., 2024. Triply periodic minimal surface structures: Design, fabrication, 3D printing techniques, state-of-the-art studies, and prospective thermal applications for efficient energy utilization. Energ. Technol. 12 (5), 2301287.
Gandy, P.J.F., Bardhan, S., Mackay, A.L., et al., 2001. Nodal surface approximations to the P, G, D and I-WP triply periodic minimal surfaces. Chem. Phys. Lett. 336 (3–4), 187–195.
Iyer, J., Moore, T., Nguyen, D., et al., 2022. Heat transfer and pressure drop characteristics of heat exchangers based on triply periodic minimal and periodic nodal surfaces. Appl. Therm. Eng. 209, 118192.
Kaur, I., Singh, P., 2021. Flow and thermal transport characteristics of Triply-Periodic Minimal Surface (TPMS)-based gyroid and Schwarz-P cellular materials. Numer. Heat Transf. A Appl. 79 (8), 553–569.
Kus, K., Wójcik, M., Malecha, Z., et al., 2024. Numerical and experimental investigation of the gyroid heat exchanger. Int. J. Heat Mass Transf. 231, 125882.

Li, W., Yu, G., Yu, Z., 2020. Bioinspired heat exchangers based on triply periodic minimal surfaces for supercritical CO2 cycles. Appl. Therm. Eng. 179, 115686.
Liu, L., Cao, Z., Shen, T., et al., 2021. Experimental and numerical investigation on flow and heat transfer characteristics of a multi-waves internally spiral finned tube. Int. J. Heat Mass Transf. 172, 121104.
Liu, L., Ma, S., Zhang, Y., et al., 2024. Parametric design of porous structure and optimal porosity gradient distribution based on root-shaped implants. Materials 17 (5), 1137.
Lv, P., Liu, L., Dong, H., et al., 2024. Charging behavior of packed-bed thermal energy storage systems in medium and low temperature applications. Appl. Energy 373, 123893.
Ma, L., Zhou, Z., Wang, J., et al., 2025. Heat transfer and flow characteristics of a novel double wall cooling design embedded by primitive-type triply periodic minimal surface structures. Int. J. Heat Fluid Flow 116, 110005.
Piedra, S., Gómez-Ortega, A., Pérez-Barrera, J., 2023. Prediction of flow properties of porous triply periodic minimal surface (TPMS) structures. Fluids 8 (12), 312.
Qin, K., Zhuang, N., Shao, C., et al., 2025. Gyroid-type TPMS structure optimization based on mathematical function control and its convective heat transfer performance study. Int. Commun. Heat Mass Transfer 162, 108682.
Qiu, N., Wan, Y., Shen, Y., et al., 2024. Experimental and numerical studies on mechanical properties of TPMS structures. Int. J. Mech. Sci. 261, 108657.
Si, T., Sun, K., Zhang, H., et al., 2025. Lattice-scale topology optimization of TPMS structure for heat transfer. Int. J. Heat Mass Transf. 251, 127288.
Sun, M., Liang, Y., Jiang, X., et al., 2025. Flow and heat transfer characteristics of anisotropic Kelvin cells: Influence of stretching ratio and mechanistic analysis. Int. Commun. Heat Mass Transfer 169, 109896.
Tang, W., Zhou, H., Zeng, Y., et al., 2023. Analysis on the convective heat transfer process and performance evaluation of Triply Periodic Minimal Surface (TPMS) based on Diamond, Gyroid and Iwp. Int. J. Heat Mass Transf. 201, 123642.
Tang, W., Guo, J., Yang, F., et al., 2024. Performance analysis and optimization of the Gyroid-type triply periodic minimal surface heat sink incorporated with fin structures. Appl. Therm. Eng. 255, 123950.
Wang, J., Jiang, X.Z., Luo, K.H., 2023. Exploring reaction mechanism for ammonia/methane combustion via reactive molecular dynamics simulations. Fuel 331, 125806.
Wang, J., Chen, K., Zeng, M., et al., 2023. Investigation on flow and heat transfer in various channels based on triply periodic minimal surfaces (TPMS). Energ. Conver. Manage. 283, 116955.
Wang, Y., Su, Z., Huang, Z., et al., 2025. Numerical study on the efficiency improvement of household thermal energy storage device by optimized finned tube heat exchanger. Appl. Therm. Eng. 126816.
Xiao, Y., Deng, H., Wang, J., et al., 2025. Numerical investigation of functional modulation in Gyroid-type TPMS structures: Convex and concave-convex geometries. Int. Commun. Heat Mass Transfer 169, 109536.
Yang, Z., Zhang, T., Li, W., et al., 2024. Experimental and numerical assessments of thermal transport in phase change material embedding additively manufactured triply periodic minimal surfaces: A comparative evaluation. Appl. Therm. Eng. 245, 122850.
Yeranee, K., Rao, Y., 2022. A review of recent investigations on flow and heat transfer enhancement in cooling channels embedded with triply periodic minimal surfaces (TPMS). Energies 15 (23), 8994.
Yeranee, K., Rao, Y., Zuo, Q., et al., 2024. Thermal performance enhancement for gas turbine blade trailing edge cooling with topology-optimized printable diamond TPMS lattice. Int. J. Heat Fluid Flow 110, 109649.
Yeranee, K., Xu, C., Rao, Y., et al., 2024. Experimental and numerical study of improving flow and heat transfer in a serpentine cooling channel with topology-optimized TPMS porous structures. Int. J. Heat Mass Transf. 231, 125873.
Yoo, D.J., 2014. Advanced porous scaffold design using multi-void triply periodic minimal surface models with high surface area to volume ratios. Int. J. Precis. Eng. Manuf. 15, 1657–1666.
Zhang, Y., Yan, Z., Shen, M., et al., 2025. Study on the thermal control performance of lightweight minimal surface lattice structures for aerospace applications. Appl. Therm. Eng. 261, 125110.
Zuo, Q., Rao, Y., Yeranee, K., 2025. Experimental and numerical study on enhanced cooling effectiveness for gas turbine blade leading edge with internal ridged swirl chamber and TPMS effusion holes. Int. J. Heat Fluid Flow 116, 109977.